

Massive stars and the energy balance of the interstellar medium. II. The $35 M_{\odot}$ star and a solution to the “missing wind problem”

Tim Freyer

Institut für Theoretische Physik und Astrophysik der Universität, D-24098 Kiel, Germany

freyer@astrophysik.uni-kiel.de

Gerhard Hensler

*Institut für Astronomie, University Observatory of Vienna, Türkenschanzstr. 17, A-1180
Vienna, Austria*

hensler@astro.univie.ac.at

and

Harold W. Yorke

*Jet Propulsion Laboratory, California Institute of Technology, MS 169-506, 4800 Oak
Grove Drive, Pasadena, CA 91109, USA*

Harold.Yorke@jpl.nasa.gov

ABSTRACT

We continue our numerical analysis of the morphological and energetic influence of massive stars on their ambient interstellar medium for a $35 M_{\odot}$ star that evolves from the main sequence through red supergiant and Wolf-Rayet phases, until it ultimately explodes as a supernova. We find that structure formation in the circumstellar gas during the early main-sequence evolution occurs as in the $60 M_{\odot}$ case but is much less pronounced because of the lower mechanical wind luminosity of the star. Since on the other hand the shell-like structure of the H II region is largely preserved, effects that rely on this symmetry become more important. At the end of the stellar lifetime 1% of the energy released as Lyman continuum radiation and stellar wind has been transferred to the circumstellar gas. From this fraction 10% is kinetic energy of bulk motion, 36% is thermal energy, and the remaining 54% is ionization energy of hydrogen. The sweeping up of the slow red supergiant wind by the fast Wolf-Rayet wind produces remarkable morphological structures and emission signatures, which are compared with

existing observations of the Wolf-Rayet bubble S308, whose central star has probably evolved in a manner very similar to our model star. Our model reproduces the correct order of magnitude of observed X-ray luminosity, the temperature of the emitting plasma as well as the limb brightening of the intensity profile. This is remarkable, because current analytical and numerical models of Wolf-Rayet bubbles fail to consistently explain these features. A key result is that almost the entire X-ray emission in this stage comes from the shell of red supergiant wind swept up by the shocked Wolf-Rayet wind rather than from the shocked Wolf-Rayet wind itself as hitherto assumed and modeled. This offers a possible solution to what is called the “missing wind problem” of Wolf-Rayet bubbles.

Subject headings: H II regions — hydrodynamics — ISM: bubbles — ISM: individual(S308) — ISM: structure — X-rays: individual(S308)

1. Introduction

In the first paper of this series (Freyer et al. 2003, subsequently referred to as Paper I) we studied the evolution of the circumstellar gas around an isolated $60 M_{\odot}$ star by means of numerical two-dimensional radiation hydrodynamic simulations. We found that the interaction of the photoionized H II region with the stellar wind bubble (SWB) strongly influences the morphological evolution during the early main-sequence (MS) phase of the star. On the one hand, the results show that the dynamical interaction processes contribute to the formation of complex structures which can be found in H II regions. On the other hand, these processes also impact on how and to what extent the stellar energy input (wind and H-ionizing radiation) is supplied to the interstellar medium (ISM), distributed among different forms of energy, and ultimately radiated from the system. While the consideration of the stellar wind strongly enhances the kinetic energy of bulk motion present in the system, ionization energy and the associated thermal energy of warm gas are generally lowered because the stellar wind intensifies the formation of high-density structures (clumps) with shorter hydrogen recombination times and stronger cooling.

With this paper we continue our numerical analysis of the morphological and energetic influence of massive stars on their ambient ISM for a $35 M_{\odot}$ star that evolves from the MS through the red supergiant (RSG) and the Wolf-Rayet (W-R) phases until it explodes as a supernova (SN). The goals of this paper are to examine the combined influence of wind and ionizing radiation on the dynamical evolution of circumstellar matter for this second set of stellar parameters, to compare and contrast the two numerical models we have obtained so far and to compare the model with observations of bubbles around W-R stars that have

undergone an RSG phase. We will complete our little sequence of circumstellar gas models for a $85 M_{\odot}$ star (D. Kröger et al. 2005, in preparation) and a $15 M_{\odot}$ star, representing the upper and lower end, respectively, of the stellar mass range that we are investigating.

The remainder of this paper has the following structure: In section 2 we review some recent observations of W-R stars with circumstellar nebulae that are conjectured to be ejected during the RSG phase of the star. Section 3 briefly reflects on the numerical methods and initial conditions used to produce the results presented in this paper and describes the set of stellar parameters used as time-dependent boundary conditions that drive the evolution. The results of the model calculations along with a comparison to observations and analytical models are presented in section 4. We summarize our main results and conclusions in section 5.

2. Recent Observations

From the theoretical point of view, each star that has a supersonic wind with a sufficiently high mass-loss rate should be capable of blowing a SWB into the ISM. The crucial indicator for the existence of such SWBs is the hot gas produced at the reverse shock. The X-ray emission of the hot ($10^6 - 10^8$ K) gas should be detectable if the surface brightness is high enough for the respective telescope in use. Although theory predicts that even massive stars on the MS are supposed to produce SWBs, they are expected to be large and diffuse with a low surface brightness in X-rays. Thus, the vicinities of W-R stars seem to be promising candidates for the observation of SWBs (also called W-R bubbles if the central star is in its W-R stage). However, only 1/4 to 1/3 of the known galactic W-R stars seem to have associated ring nebulae and only 10 are wind-driven bubbles (Wrigge 1999), according to the optically derived kinematics of the shell (Chu 1981). Up to now only 2 of these SWB candidates have actually been detected in X-rays: NGC 6888 (Bochkarev 1988; Wrigge et al. 1994) and S308 (Wrigge 1999; Chu et al. 2003). Since both central W-R stars are thought to have undergone the MS \rightarrow RSG \rightarrow W-R evolution that we are investigating in this paper, we will briefly review the recent observational work for a careful comparison with our numerical results.

NGC 6888 was among the first galactic ring nebulae whose formation have been attributed to mass ejection and radiation from a W-R star (Johnson & Hogg 1965). Its relative proximity and thus large angular size ($18' \times 12'$) has made it to one of the best studied examples of this class of objects. At a distance of 1.45 kpc (Wendker et al. 1975) the physical radius of the nebula is 3.8 pc (major axis) \times 2.5 pc (minor axis). The WN6 star HD 192163 (= WR 136 according to the list of van der Hucht 2001) is close to the center

of the nebula. The ellipsoidal shell appears to be geometrically very thin and has a highly filamentary structure. With a mean electron density in the filaments of the nebula of 400 cm^{-3} (Parker 1964), Wendker et al. (1975) derived a mass of $5 M_{\odot}$ for the ionized shell and a mean shell thickness of 0.01 pc. The shell expansion velocity varies among different authors in the range $75 - 93 \text{ km s}^{-1}$ (Treffers & Chu 1982; Marston & Meaburn 1988; Moore et al. 2000).

It is important to distinguish two morphological features that are theoretically expected to evolve during the RSG and W-R stage of the star: A thin and dense “RSG shell” forms around the outflowing RSG wind when the reverse shock becomes radiative due to the high density of the wind in this stage. When the fast W-R wind turns on, the non-radiative reverse shock reestablishes itself and the shocked W-R wind sweeps up the RSG wind in the so-called “W-R shell”. The dynamical age of the W-R shell

$$t_{\text{dyn}} = \frac{\eta R_{\text{shell}}}{v_{\text{shell}}} \quad (1)$$

depends on the expansion velocity and on the assumption of the density profile into which the shell expands. Typically, two cases are considered: a constant ambient density ($\eta = 0.6$ according to Weaver et al. 1977) and a $\rho \propto 1/r^2$ density profile ($\eta = 1.0$ according to García-Segura & Mac Low 1995). With the expansion velocities quoted above, a mean shell radius of 3.2 pc, and the assumption that the optically visible nebula can be associated with the W-R shell, one obtains a minimum value for the dynamical age of NGC 6888 of $2.0 \times 10^4 \text{ yr}$ ($\eta = 0.6$ and $v_{\text{shell}} = 93 \text{ km s}^{-1}$) and a maximum value of $4.2 \times 10^4 \text{ yr}$ ($\eta = 1.0$ and $v_{\text{shell}} = 75 \text{ km s}^{-1}$).

Moore et al. (2000) used the WFPC2 on the *Hubble Space Telescope (HST)* to examine the filaments of the bright northeast rim of NGC 6888 in the light of the $\text{H}\alpha$ $\lambda 6563$, $[\text{O III}]$ $\lambda 5007$, and $[\text{S II}]$ $\lambda \lambda 6717, 6731$ lines. They found filament densities of $1000 - 1600 \text{ cm}^{-3}$. The dense shell is enveloped by a skin of emission most evident in $[\text{O III}]$ $\lambda 5007$ and it is proposed that this skin arises in a cooling regime behind a radiative shock driven into the medium around the shell. For the low density that is expected in the MS bubble without heat conduction a forward shock ahead of the nebula shell would not be visible. Thus, the authors propose that a considerable fraction of the approximately $18 M_{\odot}$ RSG wind is possibly present in the MS bubble as a low-density (2 cm^{-3}) exterior layer with low $\text{H}\alpha$ surface brightness, visible only in $[\text{O III}]$ $\lambda 5007$ postshock emission as the skin engulfing the $\text{H}\alpha$ filaments when it becomes shocked by some combination of nebular shell expansion and the pressure of the postshock W-R wind overtaking the RSG shell. The large discrepancy between the density in the MS bubble of the model and the observed density of the skin could be explained by thermal evaporation of RSG wind material into the MS bubble. Spectroscopy of the nebular shell shows that the ionized gas is enriched with nitrogen and helium

and underabundant in oxygen. Possible explanations might be the transport of chemically enriched material from the core of the star to the outer layers that are ejected during the RSG stage (Esteban & Vílchez 1992) or the mixing of W-R and RSG wind material (Kwitter 1981). The high abundance of nitrogen in the nebula is consistent with the classification of HD 192163 as a WN6 star.

There is some debate on how much neutral gas is present in NGC 6888. The answer to this question has implications on the interpretation of the dynamics of the bubble as being either energy or momentum conserving. Marston & Meaburn (1988) found from *IRAS* observations (assuming a gas to dust mass ratio of 100) a shell of $40 M_{\odot}$ neutral gas directly outside the ionized shell. The difficulty in the interpretation of the observed data is the correct estimate of the forbidden line contribution in the far infrared. Van Buren & McCray (1988) concluded that the emission in the *IRAS* 60 μm and 100 μm bands is predominantly from forbidden [O III] lines indicating that the continuum emission from the dust and thus the neutral mass would be negligible. Marston (1991) claims that the flux contribution from forbidden [O III] and [N III] lines is only 8 – 20% and that the major reason for these deviating results is the higher flux from the nebula which he derived because of a differing background removal procedure. However, Moore et al. (2000) conclude from their *HST* WFPC2 observations of the nebula that there cannot be a significant amount of neutral material close to the optical nebula. Their result for the hydrogen ionizing flux of $10^{49.3}\text{s}^{-1}$ is in reasonable agreement with the value of 10^{49}s^{-1} from the W-R models of Crowther & Smith (1996) and does perfectly match the value from García-Segura et al. (1996) that we use for our calculations presented in this paper, but it is roughly a factor of 50 higher than the Lyman continuum flux of $10^{47.6}\text{s}^{-1}$ which Marston & Meaburn (1988) found as necessary to maintain the observed $\text{H}\alpha$ brightness of the nebula. In other words: Only 2% of the ionizing photons from HD 192163 are used to ionize the observable nebular shell of NGC 6888 - it is “density-bounded” not “ionization-bounded”. 98% would still be available to ionize the neutral parts of the shell. Since the shock front ahead of the shell is partially shadowed from the stellar Lyman continuum flux by dense clumps within the shell, it is obvious that there is indeed some neutral material in the shell, but on the other hand the shell is very leaky to Lyman continuum photons and it is unlikely that there is as much as $40 M_{\odot}$ neutral gas present directly outside the ionized shell because that would process a larger fraction of the stellar Lyman continuum flux into $\text{H}\alpha$ emission.

Observational evidence has also been found for the existence of the shell of swept-up ambient ISM around the MS bubble. Using highly resolved *IRAS* images Marston (1995) discovered an elliptical shell with average radius of 19 pc (assuming a distance to HD 192163 of 1.45 kpc) and mass of $\approx 8000 M_{\odot}$ (assuming a gas to dust mass ratio of 100). However, this value should be used with some caution since it was obtained with the same techniques

that have been applied to produce the controversial result for the amount of neutral mass contained in the W-R bubble.

NGC 6888 was the first SWB that has been observed in X-rays (Bochkarev 1988; Wrigge et al. 1994). The latter authors examined the X-ray emission from NGC 6888 using the PSPC detector of the *ROSAT* satellite and found that it is filamentary and concentrated in the brightest optical features of the nebula. 70% of the total X-ray emission originates from only $\approx 1 - 2\%$ of the bubble volume. With their assumed distance to NGC 6888 of 1.8 kpc the X-ray luminosity is estimated to be 1.6×10^{34} ergs s^{-1} in the energy band 0.07 – 2.41 keV and the plasma temperature to be 2×10^6 K. Wrigge & Wendker (2002) also used the HRI detector on board the *ROSAT* satellite to obtain X-ray emission maps with higher spatial resolution. They conclude that approximately half of the total X-ray emission originates from small filaments with typical size of a few tenths of a pc and typical luminosity in the *ROSAT* HRI band of several 10^{31} ergs s^{-1} , corresponding to a hydrogen number density in the filaments of a few cm^{-3} . Wrigge & Wendker (2002) also examined the possibility that the emission of these filaments is produced by clumps of dense gas which evaporate in the bubble of hot gas. They find that this explanation could only be consistent with the observations if the bubble gas is sufficiently hot ($5 - 10 \times 10^6$ K).

S308 surrounding the WN4 star HD 50896 (= EZ CMa = WR 6) is the second SWB that has been observed in X-rays. The optically visible nebula is characterized by an almost spherically symmetric shell with a remarkable protrusion in the northwest quadrant but otherwise with no hints on the formation of pronounced instabilities. The distance to S308 and thus all quantities which scale with the distance are somewhat uncertain. Chu et al. (1982) give $D = 1.5$ kpc. Hamann et al. (1988) found that the range from 0.9 to a few kpc is in agreement with the results of their spectral analysis, with a preferred value of 2 kpc. Howarth & Schmutz (1995) estimate $D = 1.8$ kpc with an uncertainty of 15% based on their high-resolution observations of the interstellar Na I D lines in the spectra of HD 50896 and several nearby stars. Measurements with the *Hipparcos* satellite indicated $D = 0.6_{-0.2}^{+0.4}$ kpc (Perryman et al. 1997), which seems to be unreasonably close, when compared with the other distance-estimate techniques. The photometric distance to HD 50896 is $D = 1.0 \pm 0.2$ kpc (van der Hucht 2001) and the kinematic distance based on radial velocity information (of S308 and neighboring H II regions) and Galactic rotation is $D = 1.5 \pm 0.2$ kpc (Chu et al. 2003). We will subsequently use a distance of 1.5 kpc and all the distance-depending values that we quote from other papers are scaled accordingly.

The radius of the optically visible shell is 9 pc and the shell expands with $v = 63$ km s^{-1} (Chu et al. 2003). The ionized mass of the shell is $54 M_{\odot}$ (Chu et al. 1982, scaled according to the values of radius and expansion velocity used here). The derived average hydrogen

number density of the ambient gas that has been swept up is thus $\approx 0.6 \text{ cm}^{-3}$. An interesting implication of the distance and position on the sky is that S308 lies approximately 260 pc above the galactic plane, an unusual place for a massive star. Since HD 50896 also has a compact companion, possibly the stellar remnant of a SN explosion, it has been proposed that it is a runaway star (Firmani et al. 1979). However, because the location of HD 50896 is almost central within S308 the transverse velocity of HD 50896 with respect to its shell cannot be very high. For an adopted dynamical age of the nebula of 0.14 Myr (Chu et al. 2003) the star can reach its projected displacement from the center of the bubble with a velocity of less than 7 km s^{-1} (Chu et al. 1982). There is no morphological evidence for supersonic transverse motion of the star + shell system with respect to its local ISM.

Wrigge (1999) used the *ROSAT* PSPC detector to examine the X-ray emission from S308. Despite some technical difficulties he found that the observed spectrum can be fitted by a two-temperature emission model, one component at $T = 1.5 \times 10^6 \text{ K}$ and the second at $T = 2.8 \times 10^7 \text{ K}$. A total luminosity of $2.1 \times 10^{33} \text{ ergs s}^{-1}$ (scaled to the distance of $D = 1.5 \text{ kpc}$) in the energy band between 0.1 keV and 2.04 keV has been determined. The emitting volume is probably a thick shell with a ratio of inner to outer radius ≈ 0.5 .

One of the major conclusions of Wrigge (1999) regarding the theoretical models is that S308 cannot be described by either the Weaver et al. (1977) constant ambient density model or by the two-wind model of García-Segura & Mac Low (1995). A comparable bubble produced within the two-wind framework would have an X-ray luminosity of $9 \times 10^{33} \text{ ergs s}^{-1}$, which is roughly in agreement with the observed value (bearing in mind the uncertainty in the determination of the observed X-ray luminosity). The problem is that the stellar wind luminosity which is necessary to reproduce the bubble in the model is only $\approx 3\%$ of the stellar wind luminosity that Hamann et al. (1993) derived for HD 50896 ($v_w = 1700 \text{ km s}^{-1}$, $\dot{M}_w = 5.4 \times 10^{-5} M_\odot \text{ yr}^{-1}$, scaled to the distance of $D = 1.5 \text{ kpc}$ used here). Even if the lower clumping-corrected mass-loss rate of Nugis et al. (1998) is used to derive the mechanical wind luminosity, the value from the model is still almost an order of magnitude lower. This is called the “missing wind problem”. Moreover, the observed X-ray surface brightness profile of S308 is limb brightened while the theoretical profile is centrally filled. The result for the classical bubble model according to Weaver et al. (1977) is similar: Although the stellar wind luminosity needed to reproduce the observed bubble kinematics is higher than in the two-wind model of García-Segura & Mac Low (1995), it is still only $\approx 8\%$ of the observed value ($\approx 32\%$ for the clumping-corrected mass-loss rate).

Chu et al. (2003) observed the X-ray emission from the northwest quadrant of S308 using the EPIC CCD cameras of the *XMM-Newton* satellite. They found that the X-ray emission is completely interior to the optical shell and reconfirmed the limb brightening.

The brightest X-ray emitting regions are linked to bright optical filaments. The total X-ray luminosity of S308, extrapolated from the observed flux from the northwest quadrant, is $\leq (1.2 \pm 0.5) \times 10^{34}$ ergs s^{-1} in the energy band between 0.25 keV and 1.5 keV. The observed spectrum can be fitted with the emission of an optically thin, nitrogen-enriched plasma of temperature $T = 1.1 \times 10^6$ K. This is quite “cool” compared to the postshock temperature of order 10^8 K which is expected for a rare stellar wind with terminal velocity of a few 1000 km s^{-1} and might indicate that the shocked W-R wind has mixed with cold gas by the processes of thermal evaporation and/or dynamic ablation. The spectrum is very soft so that there is basically no emission beyond 1 keV. The existence of a high-temperature gas component that substantially contributes to the observed emission and that has been claimed to be detected by Wrigge (1999) is ruled out. Less than 6% of the observed X-ray flux (which corresponds to 1.5% of the unabsorbed X-ray flux) can be attributed to the emission of a hotter gas component. The reason for these contradicting results is probably the low signal-to-noise ratio in the *ROSAT* PSPC data that Wrigge (1999) obtained together with a number of point sources which have not been resolved by the PSPC detector. Since the [O III] $\lambda 5007$ emission of S308 has a sharp rim, the nebular shell is probably still surrounded by unaffected RSG wind material. This RSG material cannot extend too much farther out, if the protrusion in the northwest quadrant is interpreted as a first blowout. There is a gap between the outer rim of the [O III] $\lambda 5007$ emission and the outer edge of the X-ray emission of between 90 arcsec to over 200 arcsec, corresponding to 0.7 – 1.5 pc. Chu et al. (2003) interpret this gap as being filled by the W-R shell and probably a transition layer. This is also indicated by the detection of an interstellar N v absorption line toward HD 50896, which Boroson et al. (1997) attribute to the shell of S308.

The electron density in the X-ray emitting gas is estimated to be $n_e = 0.28 \pm 0.04$ cm^{-3} or $n_e = 0.63 \pm 0.09$ cm^{-3} for an assumed hot gas volume filling factor of 0.5 or 0.1, respectively. The filling factor is expected to be closer to 0.5 since the limb-brightened X-ray emission profile suggests emission from a thick shell. The resulting mass of the X-ray emitting gas is $11 \pm 5 M_\odot$ or $5 \pm 3 M_\odot$ for the two volume filling factors. Assuming that the optical emission which has been used to determine the expansion velocity comes from the W-R shell, the age of the W-R phase can be estimated using equation 1. For $R_{shell} = 9$ pc, $v_{shell} = 63$ km s^{-1} , and $\eta = 1.0$ this yields $t_{dyn} = 0.14$ Myr. For a clumping-corrected mass-loss rate of HD 50896 of $1.4 \times 10^{-5} M_\odot$ yr^{-1} (Nugis et al. 1998, scaled to the distance used here) the mass blown into the bubble by the W-R wind is $2 M_\odot$. This is less than the X-ray emitting gas mass, a fact which in turn supports the idea that RSG material is mixed with the shocked W-R wind in the bubble or that the main source of X-rays is different from the shocked W-R wind. Observations of S308 in the optical waveband furthermore show that besides photoionization there is also shock heating present, indicated by the high [O III] $\lambda 5007/H\beta$

ratio of 20 (Esteban et al. 1992). Similar to the case of NGC 6888, the [O III] $\lambda 5007$ emission leads the H α emission by 16-20 arcsec (Gruendl et al. 2000) corresponding to 0.12 – 0.15 pc. Furthermore, S308 is located in an H I cavity swept free by the MS wind of HD 50896 (Arnal & Cappa 1996).

3. Numerical Method

3.1. Radiation Hydrodynamics Scheme

The numerical code used to obtain the results presented in this paper is described in Paper I. The hydrodynamical equations are solved together with the transfer of H-ionizing photons on a two-dimensional cylindrical grid. The time dependent ionization and recombination of hydrogen is calculated each time step and we carefully take stock of all the important energy exchange processes in the system. For a closer description of the algorithm we refer the reader to Yorke & Kaisig (1995), Yorke & Welz (1996), and Paper I.

3.2. Initial Conditions

We use the same undisturbed background gas layer with hydrogen number density $n_0 = 20 \text{ cm}^{-3}$ and temperature $T_0 = 200 \text{ K}$ for the reasons described in Paper I and start our calculations with the sudden turn-on of the zero-age main-sequence (ZAMS) stellar radiation field and stellar wind. After $t = 700 \text{ yr}$ the spherical one-dimensional solution is used as initial model for the two-dimensional calculations.

3.3. Boundary Conditions

The basic difference between the $60 M_\odot$ case described in Paper I and the $35 M_\odot$ case is the set of time-dependent stellar parameters. The mass-loss rate (\dot{M}_w), terminal velocity of the wind (v_w), effective temperature (T_{eff}), and photon luminosity in the Lyman continuum (L_{LyC}) drive the evolution of the circumstellar gas. For the $35 M_\odot$ star we adopt the stellar parameters given by García-Segura et al. (1996, their version with the “fast” 75 km s^{-1} RSG wind) shown in Figure 1. Here, the star undergoes the following evolution: MS O star \rightarrow RSG star \rightarrow W-R star \rightarrow SN. The MS phase lasts for about 4.52 Myr, the RSG phase 0.234 Myr and the final W-R phase 0.191 Myr. After 4.945 Myr the calculation stops and the star explodes as a SN.

During the star’s MS phase the mass-loss rate rises approximately from $3 \times 10^{-7} M_{\odot} \text{ yr}^{-1}$ to $10^{-6} M_{\odot} \text{ yr}^{-1}$. With the onset of the RSG phase the mass-loss rate jumps up to almost $10^{-4} M_{\odot} \text{ yr}^{-1}$. In the final W-R phase it is of the order $(2-3) \times 10^{-5} M_{\odot} \text{ yr}^{-1}$. The terminal velocity of the stellar wind on the MS is between $2 \times 10^3 \text{ km s}^{-1}$ and $4 \times 10^3 \text{ km s}^{-1}$, during the RSG phase it drops below 100 km s^{-1} until it again reaches values of $(1-4) \times 10^3 \text{ km s}^{-1}$ in the final W-R phase. The effective temperature during the MS phase lies in the range of $(3-4) \times 10^4 \text{ K}$, falls down to a few thousand Kelvin in the RSG phase and temporarily reaches more than 10^5 K during the final W-R phase. While the total photon luminosity of the star is relatively constant with values of $(7-14) \times 10^{38} \text{ ergs s}^{-1}$ during the whole evolution of the star, the photon luminosity in the Lyman continuum and the mechanical luminosity of the wind reflect the strong changes of mass-loss rate, terminal velocity of the wind and effective temperature. The Lyman continuum luminosity during the MS is in the range of $(2-3) \times 10^{38} \text{ ergs s}^{-1}$. In the course of the RSG phase it is insignificant due to the strong decrease of the effective temperature. The inverse situation occurs during the subsequent W-R phase: Because of the high effective temperature, most of the radiative power is emitted above the Lyman edge and the Lyman continuum luminosity reaches almost $10^{39} \text{ ergs s}^{-1}$. The mechanical wind luminosity ($\dot{M}_w v_w^2/2$) during the MS phase is $(1-2) \times 10^{36} \text{ ergs s}^{-1}$, drops by approximately one order of magnitude during the RSG phase, and reaches the highest values between $10^{37} \text{ ergs s}^{-1}$ and $10^{38} \text{ ergs s}^{-1}$ in the final W-R phase.

Here, the radius of the “wind generator region” is $2.16 \times 10^{17} \text{ cm}$. The grid organization scheme as well as the other boundary conditions are unchanged compared to the $60 M_{\odot}$ case presented in Paper I.

3.4. Geometry and Resolution

The size of the coarsest mesh, representing the size of the computational domain, is $r_{\text{max}} = z_{\text{max}} = 50 \text{ pc}$. This value ensures that the coarsest grid covers the entire evolution during the lifetime of the star and thus prohibits that the ionization front or moving material can reach the outer boundary of the coarsest grid. The size is smaller than for the $60 M_{\odot}$ case since the size of the developing bubble is smaller as well. Six nested grids are employed within the coarsest grid, resulting in seven grid levels. On each grid level 125×125 cells (excluding ghost cells) are used resulting in a linear resolution that ranges from $6.25 \times 10^{-3} \text{ pc}$ close to the star to 0.4 pc in the outermost parts of the coarsest grid.

4. Results and Discussion

4.1. A Resolution Study

Similar to Paper I we performed a resolution study for the $35 M_{\odot}$ case to ensure that the spatial resolution is high enough and that the numerical results are trustworthy. The same selection of parameters was calculated with three different resolutions, medium (125 cells in each dimension), low (61 cells in each dimension), and high (253 cells in each dimension). Again, we compare only the first Myr of the evolution since the high-resolution model would require too much CPU time for the entire lifetime of the star. Figure 2 shows the results of this resolution study.

The quality of the results is comparable to that of the $60 M_{\odot}$ case presented in Paper I. The variation of the thermal energy with resolution is $\lesssim 0.05$ dex at almost any time during the first Myr. For ionization energy and kinetic energy of bulk motion the deviation between low and high resolution is $\lesssim 0.05$ dex for $0.5 \text{ Myr} \leq t \leq 1.0 \text{ Myr}$ and $\lesssim 0.1$ dex for $t \leq 0.5 \text{ Myr}$, the latter case with a considerably smaller shift between medium and high resolution than between low and medium resolution, indicating that these values are already close to the actual limit. These results show that for the $35 M_{\odot}$ case discussed here the errors in our energetic analysis due to resolution effects are within an acceptable range, while there are morphological details which remain to be explored in future simulations with even higher resolution.

4.2. Evolution of the $35 M_{\odot}$ Case

Figures 3 to 15 depict the evolution of the gas in the vicinity of and under the influence of the $35 M_{\odot}$ model star. The data are plotted in the same manner as in Paper I for the $60 M_{\odot}$ case. Once again, we begin our discussion with the initial model that has been set up from the one-dimensional solution. For the $35 M_{\odot}$ case this is done after 700 yr because — due to the lower mechanical wind luminosity of the star — the pressure in the hot bubble is lower. Thus, the forward shock is weaker and the shell of swept-up material is less heated and collapses earlier.

As expected, the basic structure of the SWB/H II region seen in Figure 3 is the same as for the $60 M_{\odot}$ case except for the length and time scales. The stellar wind flows with the terminal velocity of nearly 4000 km s^{-1} freely out to $r \approx 0.08 \text{ pc}$, the position of the reverse shock, where it is heated up to about 10^8 K . The forward shock that sweeps up the H II region is at $r \approx 0.23 \text{ pc}$ and moves with some 130 km s^{-1} . Density and temperature

immediately behind this shock front are $\rho \approx 1.4 \times 10^{-22} \text{ g cm}^{-3}$ and $T \approx 2.5 \times 10^5 \text{ K}$, respectively, which is in good agreement with the jump conditions for a strong shock moving into photoionized gas with $T \approx 8000 \text{ K}$. The ionization front is still weak R-type at 4.7 pc.

After $5 \times 10^4 \text{ yr}$ (Figure 4) the hot bubble extends out to about 2.3 pc. The shell of swept-up H II region expands with some 24 km s^{-1} . Density knots have been produced in the thin shell, similar to those seen in the $60 M_{\odot}$ case, altering the optical depth along different radial lines of sight. The H II region has begun to expand with almost 10 km s^{-1} , sweeping up the ambient neutral gas, but the ionization front has started to retreat at the places where the clumps in the stellar wind shell cast shadows into the H II region. The basic morphological structure is still comparable to the $60 M_{\odot}$ case.

Figure 5 shows the evolutionary state of the $35 M_{\odot}$ case after 0.2 Myr. The radius of the H II region is approximately 9.5 pc and it expands into the ambient medium at several km s^{-1} . (When neutral shadows and ionized extensions appear, we define the radius of the H II region as the distance from the star to the “undisturbed” ionization front which is neither extended along the fingers nor shortened by the shadows.) The hot bubble has grown to $r \approx 4.8 \text{ pc}$ and the expansion velocity of the stellar wind shell has decelerated to $\approx 13 \text{ km s}^{-1}$. This is comparable to the sound speed in the H II region; i.e., the outermost side of the stellar wind shell is no longer bound by a shock front and has begun to expand into the H II region as a result of the pressure gradient between the shell and the H II region. (For clarity, we distinguish the stellar wind shell and the H II region. Actually, the stellar wind shell is an important part of the H II region because it is, at least at this point in time, photoionized by the star.) At $t = 0.2 \text{ Myr}$ the geometrical thickness of the stellar wind shell has already grown to 1 pc and the density in the shell is $(6 - 9) \times 10^{-23} \text{ g cm}^{-3}$.

As a result of the growth of the geometrical shell thickness, the thin-shell instability that triggered the formation of density clumps in the shell ceased and the clumps dissolved; the period of time they were present in the stellar wind shell was relatively short. Thus, the shadows in the H II region are much less pronounced and the finger-like extensions of the H II region are shorter and less numerous than for the $60 M_{\odot}$ case. Nevertheless, density fluctuations in the H II region of more than an order of magnitude have been produced. (This may be a lower limit because of restrictions in resolution.) Maximum densities are around $\rho \approx 5 \times 10^{-23} \text{ g cm}^{-3}$ and minima around $\rho \approx 3 \times 10^{-24} \text{ g cm}^{-3}$. At these densities, temperatures, and masses the clumps are not gravitationally bound.

The dissolution of the stellar wind shell can impressively be seen in Figure 6 at $t = 0.3 \text{ Myr}$. The expansion of the stellar wind shell has become a 2 pc broad belt of outflow with density $(2 - 5) \times 10^{-23} \text{ g cm}^{-3}$ from the contact discontinuity at $r \approx 6 \text{ pc}$ into the H II region with about sound speed.

Additional processes are triggered by the rarefaction of the gas that previously belonged to the stellar wind shell: Because of the increase of hydrogen recombination time with lower density, excess photons are generated which reionize the shadowed regions (see lower panel of Figure 6) and advance the ionization front even further, evaporating additional material from the H II region shell of swept-up ambient medium ahead. This evaporation is visible in the density increase and the disturbed velocity field in the outer parts of the H II region close to the ionization front. As a transient phenomenon, another shell with a density of $(3 - 6) \times 10^{-23} \text{ g cm}^{-3}$ develops at $t \approx 0.35 \text{ Myr}$ when the former stellar wind shell gas flowing into the H II region collides with the photoevaporated material from this swept-up ambient shell.

Together with the relics of denser fragments in the H II region, the larger opacity in this dense shell causes once again the formation of small ripples in the ionization front at $t \approx 0.4 \text{ Myr}$ (Figure 7). At this time the radius of the hot bubble is about 7.5 pc and the geometrical thickness of the whole H II region is about 4 pc. However, the newly formed shell soon dissolves because of its overpressure with respect to the rest of the H II region, and within certain limits it can thus be said that the dissolution of the stellar wind shell leads to a “rehomogenization” of the H II region.

If we continue our analysis of this case to $t = 0.6 \text{ Myr}$ (Figure 8, please note the different scale), we see that the hot bubble has grown to almost 10 pc in radius. The shell-like H II region, still expanding into the ambient medium at about 10 km s^{-1} , becomes more and more homogeneous. Nevertheless, remaining density fluctuations from the previous formation and destruction processes are still in the range from $7 \times 10^{-24} \text{ g cm}^{-3}$ to $4 \times 10^{-23} \text{ g cm}^{-3}$.

We compare the morphological characteristics of the circumstellar gas which result from our runs with different resolution after 1 Myr in Figure 9 (high resolution) and Figure 10 (medium resolution). As can be expected the overall structure in both runs is the same. The radius of the shell of swept-up ambient gas around the H II region is $\approx 17 \text{ pc}$ and it expands at almost 10 km s^{-1} . The geometrical thickness of the H II region itself is slightly larger in the high-resolution run, the velocity field in the H II region is stronger perturbed than in the medium-resolution run, and some fragments of the photoionized gas protrude and get mixed into the hot gas. All the latter deviations can be understood in terms of the finer substructures in the H II region, which were able to form in the high-resolution run. However, the trend toward a rehomogenization of the H II region continues: The density fluctuations in the H II region are only in the range of $9 \times 10^{-24} \text{ g cm}^{-3}$ to $2 \times 10^{-23} \text{ g cm}^{-3}$, except for very small regions at the inner side of the shell of swept-up ambient gas. Here the density is reduced after neutral clumps from the shell have been evaporated “explosively”. Subsequently for $t > 1 \text{ Myr}$ we consider only the medium-resolution model.

Since the stellar parameters vary only very gradually during the MS phase until the star enters the RSG stage (see Figure 1), the basic structure of the SWB/H II region remains the same during the next 3 Myr except that it continues to grow. Thus, we can proceed with our description of the evolution to Figure 11, which shows the bubble at the age of 4 Myr (please note once again the larger scale). The radius of the hot bubble is now about 27 pc and the H II region extends out to ≈ 35 pc. The hot bubble and the photoionized H II region are in pressure equilibrium; as the pressure of the hot bubble decreases through expansion, the pressure of the H II region drops, too. Because the temperature in the H II region is nearly constant in time, the density has decreased to $(3.9 - 5.5) \times 10^{-24}$ g cm $^{-3}$. A few dense clumps are visible in the hot bubble which have detached from the H II region. The thermal pressure of the SWB/H II region is still ≈ 20 times higher than that of the ambient medium and the whole structure still expands at about 4 – 5 km s $^{-1}$. As a result of the additionally swept-up material, the reduced pressure in the H II region, and the deceleration of the expansion, the geometrical thickness of the outer shell has increased to almost 3 pc while its density has decreased to $\rho \approx (1 - 2) \times 10^{-22}$ g cm $^{-3}$. Thus, the mass collected in this shell is about 2×10^{38} g. This result is in good agreement with the picture that most of the ambient gas that has been swept up during the expansion since the ionization front turned to D-type is still stored in the outer shell and that only a minor fraction has been evaporated into the H II region.

At $t \approx 4.52$ Myr the star enters the RSG phase. The effective temperature of the star decreases to a few thousand Kelvin and the Lyman continuum flux drops by many orders of magnitude. The mass-loss rate strongly increases and the terminal velocity of the wind decreases; i.e., the star blows a dense and slow wind into the hot bubble. This can be seen in Figure 12, which depicts the state of the circumstellar gas at $t \approx 4.59$ Myr. At this time the dense RSG wind fills the inner 5 pc of the volume and expands at about 90 km s $^{-1}$ into the hot bubble extending out to about 30 pc. Although the wind speed during the RSG phase is relatively low (compared to the MS and W-R phases), the material becomes shocked when it is decelerated by the pressure of the MS bubble because the sound speed in the RSG wind is also low. (The gas is cold and neutral, or even molecular, because the soft stellar radiation field in the RSG phase is incapable of ionizing and heating it.) Since the density of the RSG wind is fairly high, this reverse shock is radiative and forms the very thin and dense RSG shell, which is not completely resolved in our calculation (compare to García-Segura et al. 1996, the case of the fast RSG wind). Because of the reduction of Lyman continuum flux, the hydrogen in the former H II region between $30 \text{ pc} \lesssim r \lesssim 38 \text{ pc}$ starts to recombine. The degree of hydrogen ionization drops to ≈ 0.3 as the gas cools from about 6600 K at $t = 4$ Myr to 4800 K. Thus, the thermal pressure in the (former) H II region drops significantly, leading to a further broadening and slowing down of the outer shell of swept-up ambient medium,

which at this time has a thickness of about 3 pc and a velocity of $\approx 4 \text{ km s}^{-1}$.

The transition from the RSG phase of the star to the W-R phase occurs at $t \approx 4.754 \text{ Myr}$. In the W-R phase the mass-loss rate is somewhat lower than in the RSG stage (see Figure 1), but the terminal velocity of the W-R wind is much higher (a few thousand km s^{-1}). The mechanical luminosity of the W-R wind is thus much higher than that of the RSG wind. Because of the increase of effective temperature to about 10^5 K , the stellar photon output occurs largely beyond the Lyman continuum limit; the star’s Lyman continuum luminosity $\approx 10^{39} \text{ ergs s}^{-1}$ is higher than during the MS phase of the star. Figure 13 shows the structure of the circumstellar gas at $t = 4.78 \text{ Myr}$, some $2.6 \times 10^4 \text{ yr}$ after the start of the W-R wind. The fast (and thus less dense) W-R wind reestablishes a non-radiative reverse shock that heats the W-R wind to about 10^8 K . The expansion of the hot gas sweeps up the slow RSG wind in the W-R shell. The expansion velocity of the W-R shell is high, almost 400 km s^{-1} . Therefore, a strong shock ahead of the W-R shell heats the RSG wind material and the W-R shell is thick (of the order 1 pc) and hot ($\approx 10^6 \text{ K}$).

Figure 13 pinpoints the moment when the W-R shell and the RSG shell collide so that only one shell of swept-up RSG wind is visible within the MS bubble (see García-Segura et al. 1996). (The shell distortion at the z -axis is a result of the dense clump that has been there before.) Stellar Lyman continuum photons ionize the RSG wind gas (before it is shock heated by the W-R shell) and reionize the former H II region, which can be seen by comparison of the lower panels of Figures 12 and 13.

As long as the W-R shell moves through the RSG wind material, the thermal pressure of the shocked W-R wind inside the W-R shell is counterbalanced by the ram pressure of the RSG material it sweeps up. When the shock passes over the boundary between the RSG and MS winds and moves into the lower density medium, it speeds up as a rarefaction wave travels back into the W-R shell. It is the overpressure of the shocked rarefied W-R gas which is accelerating the much denser W-R shell. This is the classical case of a Rayleigh-Taylor unstable configuration and the W-R shell is torn into long filaments as the shocked W-R wind breaks through it. This can be seen very impressively in Figure 14 at $t = 4.80 \text{ Myr}$.

Figure 15 shows the final, pre-supernova state of the circumstellar gas after 4.945 Myr of evolution. The wind flows freely out to 9 – 10 pc. This value is somewhat uncertain, however, due to the very complex flow pattern. The freely flowing wind is surrounded by the hot bubble that extends out to 31 – 37 pc (on average 34 pc). The gas density in the hot bubble is $(1 - 30) \times 10^{-27} \text{ g cm}^{-3}$. This is fairly high (compared to the density at the end of the MS phase of the star) because some of the RSG/W-R ejecta mixes with the hot bubble gas, enhancing the density significantly and lowering the temperature.

The thickness of the shell-like H II region has shrunk to 3 – 8 pc with an average of 5.5 pc, after the RSG ejecta hit it and the pressure in the hot bubble has risen. This also enhances the density in the H II region to $(2 - 20) \times 10^{-24} \text{ g cm}^{-3}$. The higher spread is a result of the higher W-R Lyman continuum flux (compared to the MS phase), leading to increased photoevaporation of the swept-up ambient material. Finally, the shell of swept-up ambient gas is 3 – 4 pc thick and the gas density in the shell is $(1 - 2) \times 10^{-22} \text{ g cm}^{-3}$. The expansion velocity of this shell is 3 – 4 km s⁻¹ and therefore still supersonic with respect to the cold ambient ISM. The outermost shock moving into the ISM heats the swept-up ISM gas to almost 10³ K. Thus, the whole structure extends out to a distance of 43 – 44 pc from the star at this evolutionary time.

4.3. The Energy Balance in the Circumstellar Gas

4.3.1. Numerical Results

We discuss the energization of the circumstellar gas around the 35 M_{\odot} star on the basis of Figure 16 and compare it with its counterpart for the 60 M_{\odot} case (Figure 17 in Paper I). The plot shows selected energy contributions in the circumstellar gas as a function of time, namely the kinetic energy of bulk motion in the whole computational domain, the ionization energy (13.6 eV per ionized hydrogen atom), the thermal energy of cold ($T \leq 10^3$ K), warm ($10^3 \text{ K} < T < 10^5$ K), and hot ($T \geq 10^5$ K) gas, respectively.

The ionization energy dominates after several thousand years, when the ionization front reaches the Strömgren radius. Here, it attains a value of approximately 3.1×10^{49} ergs, which is about half an order of magnitude less than for the 60 M_{\odot} case due to the lower Lyman continuum luminosity of the 35 M_{\odot} star. The subsequent dip in ionization energy is much less pronounced than for the 60 M_{\odot} case, since at that time there is less structure formation in the H II region, as is evident in Figures 5 through 7. Afterward, the ionization energy rises smoothly to 1.8×10^{50} ergs before the star enters the RSG stage. During the RSG stage the ionization energy drops by an order of magnitude since the H-ionizing radiation from the star is completely switched off and the photoionized gas recombines. The gas is reionized when the star evolves to the W-R phase; the ionization energy reaches a global maximum of 2.8×10^{50} ergs. Contrary to the 60 M_{\odot} case, the ionization energy remains the dominant form of energy in the system for the entire evolution except for a brief period at the end of the RSG phase.

A feature which we already described for the 60 M_{\odot} case can also be seen in the 35 M_{\odot} case: The evolution of the thermal energy of warm gas follows that of the ionization

energy over the lifetime of the star with a shift of 0.7 – 0.9 dex due to the fact that for both cases, photoionization is responsible for the bulk production of ionized gas at typically 8000 K. The shift is smaller during the RSG phase of the star because cooling is less efficient in the formerly photoionized regimes when the hydrogen recombines and the plasma becomes neutral.

The evolution of the kinetic energy of bulk motion and the thermal energy of hot gas are also very similar; they do not deviate from each other by more than 0.2 dex until the star enters the RSG phase. Whereas the kinetic energy remains basically constant during the RSG phase, the thermal energy of hot gas decreases as the supply of hot gas by the reverse shock dies off. The cooling of the hot gas and mixing with cooler gas continues. Both values rise when the non-radiative reverse shock reestablishes itself in the W-R phase. When the calculations are stopped, the kinetic energy is 4.9×10^{49} ergs and the thermal energy of hot gas 1.1×10^{50} ergs; the latter value is almost the same as at the end of the $60 M_{\odot}$ calculation at 4.065 Myr.

The thermal energy of cold quiescent gas in the entire computational domain at the beginning of the calculation is 1.6×10^{49} ergs (the same energy density as in the $60 M_{\odot}$ case, but with a smaller computational volume). This value grows smoothly during the lifetime of the star as more and more ambient gas becomes swept up and weakly shocked by the outer shell. The thermal energy of the cold gas at the end of the calculation is 3.5×10^{49} ergs; i.e., 1.9×10^{49} ergs have been added during the evolution.

To study the impact of the stellar wind on the energy transfer in the circumstellar gas, we compare the energy in the system as a function of time for the two cases: 1) the standard case with wind and 2) the H II region evolution without wind (Figure 17, see also Figure 18 in Paper I). The kinetic energy of bulk motion is enhanced due to the added kinetic energy of the stellar wind shell. On the other hand, the compression of the H II region into a shell with higher density reduces the amount of ionization energy stored in the system compared to the windless case. Thus, the ratio of ionization energy for the calculation with wind to that of the windless model is below 1 throughout the lifetime of the star. Both features are well recognized from the $60 M_{\odot}$ case. In general, the deviations of the energies between the models with and without stellar wind are smaller in the $35 M_{\odot}$ case, especially during the MS evolution. For most of the MS time the ratios are well within the interval 0.5 – 2.0. This difference to the $60 M_{\odot}$ case exists because the ratio of mechanical luminosity to Lyman continuum luminosity of the $35 M_{\odot}$ star is smaller than that of the $60 M_{\odot}$ star.

There is a drop in the ratio of the ionization energies with and without wind during the RSG phase of the star. At first glance, this is surprising since in the calculation with stellar wind there is additional ionization energy in the hot bubble. But the density in the

hot bubble is very low and although the thermal energy of the hot gas in the bubble is important, there is not much ionization energy involved. The reason for the drop in the ratio of the ionization energies with and without wind is the fact that in the calculation with wind the H II region is compressed into a shell surrounding the hot bubble and the density in this shell is higher than in the spherical H II region of the windless simulation. The higher density results in shorter recombination times and thus a faster loss of ionization energy when the Lyman continuum radiation of the star ceases at the beginning of the RSG phase.

Due to the acceleration of the slow RSG wind by the shocked W-R wind, there is a strong peak in the ratio of the kinetic energies with and without wind. This additional kinetic energy is partially dissipated when the accelerated RSG wind material hits the H II region. At the end of the simulation the kinetic energy in the calculation with stellar wind is enhanced by 85%, whereas the ionization energy is reduced by 34%, and the thermal energy that is added to the system during the evolution is increased by 88% compared to the calculation without stellar wind.

One of the goals of this work is to determine the efficiencies with which the stellar input energy is converted into the different forms of energy in the circumstellar medium. We show these values for the $35 M_{\odot}$ case in Figure 18 (compare Figure 21 in Paper I). We recall here that we define the transfer efficiency as the cumulative fraction of the stellar input energy that has been converted into a particular form of energy in the circumstellar medium up to the time $t = \tau$, where τ is the age of the star. Figure 18 shows the transfer efficiencies into kinetic, ionization, and thermal energy and their sum for the $35 M_{\odot}$ case.

As we have already seen in Figure 16, the energization of the circumstellar gas occurs fairly smoothly until the star reaches the RSG stage. The transfer efficiency into kinetic energy reaches 5.6×10^{-4} before and during the RSG phase and peaks up to 2.2×10^{-3} when the shocked W-R wind accelerates the RSG wind. At the end of the simulation it is 10^{-3} . The transfer efficiency into thermal energy is higher than that into kinetic energy by a factor of 2 to 3 during most of the MS time. It reaches 1.4×10^{-3} before the RSG phase, drops by almost a factor of 2 during the RSG phase, rises again when the star enters the W-R stage, and ends up at 3.6×10^{-3} at the end of the simulation. The transfer efficiency into ionization energy is the highest except during the RSG stage of the star. Before the RSG phase it is 4.4×10^{-3} and at the end of the simulation it is 5.5×10^{-3} .

The total energy transfer efficiency (into kinetic, thermal, and ionization energy) at the end of the simulation is 10^{-2} ; i.e., 1% of the total input energy from the star is transferred to the circumstellar gas. This is comparable to the net efficiency of the windless simulation. This result shows that, globally speaking, the role of the stellar wind is less important than for the $60 M_{\odot}$ case where its presence doubled the total energy transfer efficiency at the

end of the calculation. However, the total energy transfer efficiency at the end of the $35 M_{\odot}$ calculation is 2.7 times as high as for the $60 M_{\odot}$ case. Since the circumstellar energy in the $35 M_{\odot}$ case is dominated by ionization energy, a substantial fraction will be lost quickly when the star ultimately turns off. On the other hand, the SN will inject a huge amount of additional energy into the circumstellar gas. Both processes are beyond the scope of this paper.

We summarize the values of the individual energy components (E_k , E_i , $E_{t,\text{cold}}$, $E_{t,\text{warm}}$, and $E_{t,\text{hot}}$) at the end of the $35 M_{\odot}$ simulations with and without stellar wind in Table 1. The values of the energy transfer efficiency into kinetic energy (ε_k), ionization energy (ε_i), thermal energy (ε_t), and their sum (ε_{tot}) at the end of the $35 M_{\odot}$ simulations with and without stellar wind are given in Table 2. For comparison purposes the corresponding $60 M_{\odot}$ results from Paper I are also given there. During the lifetime of the $35 M_{\odot}$ star, the total energy emitted in the Lyman continuum is $E_{\text{LyC}} = 4.61 \times 10^{52}$ ergs and the mechanical energy of the stellar wind amounts to $E_w = 4.77 \times 10^{50}$ ergs.

4.3.2. Comparison with Analytical Results

Taking mean values for the relevant stellar parameters over the lifetime of the $35 M_{\odot}$ star, we can calculate the kinetic, ionization, and thermal energy in the system according to the analytical solutions given in § 2 of Paper I. With $\langle T_{\text{eff}} \rangle = 3.78 \times 10^4$ K, $\langle L_{\text{LyC}} \rangle = 2.95 \times 10^{38}$ ergs s^{-1} , and using $\alpha_B = 3.37 \times 10^{-13}$ $\text{cm}^3 \text{s}^{-1}$ as hydrogen recombination coefficient and $c_{s,\text{HII}} = 1.15 \times 10^6$ cm s^{-1} for the isothermal sound speed in the H II region (corresponding to $T_{\text{HII}} = 8000$ K), we obtain for $n_0 = 20 \text{ cm}^{-3}$ after $\tau = 4.945$ Myr from equations (3), (4), and (5) in Paper I for the $35 M_{\odot}$ case without wind:

$$\begin{aligned} E_k &= 2.7 \times 10^{49} \text{ ergs} , \\ E_i &= 2.9 \times 10^{50} \text{ ergs} , \\ E_t &= 4.5 \times 10^{49} \text{ ergs} . \end{aligned}$$

With the same definition of the energy transfer efficiency according to equation (11) in Paper I we get the corresponding energy transfer efficiencies in the analytical approach:

$$\begin{aligned} \varepsilon_k &= 5.8 \times 10^{-4} , \\ \varepsilon_i &= 6.4 \times 10^{-3} , \\ \varepsilon_t &= 9.7 \times 10^{-4} . \end{aligned}$$

The analytical value for the transfer efficiency into kinetic energy deviates from the numerical result by less than 2%. Bearing in mind all the approximations which were made

in order to obtain the analytical solution, it is clear that the almost perfect correspondence between analytical and numerical result is certainly by chance. This is supported by the fact that the numerical value for ε_k is almost constant during most of the MS and RSG lifetime, but jumps up by $\approx 40\%$ during the final W-R stage. Analytical and numerical results for the transfer efficiency into thermal energy show fairly good correspondence immediately before the RSG phase (not shown here), but since the final W-R stage boosts the thermal energy and thus also the transfer efficiency into thermal energy, the final value deviates from the analytical one by approximately a factor of 2. The comparison of analytical and numerical results for the transfer efficiency into ionization energy bears similar results. The values are fairly close to each other before the star turns to the RSG stage, and the deviation at the end of the simulation is also only $\approx 30\%$.

As we have already discussed in Paper I, the comparison of analytical with numerical results is much more difficult in the case of the combined SWB/H II region calculation because no analytical solution is yet known for energy transfer efficiencies in the case of H II regions with stellar winds. Again, we construct an analytical approximation by simply adding up the energy contributions from the H II region and the SWB, bearing in mind that this is only a rough estimation which actually neglects the mutual interactions. In any case the analytical energy transfer efficiencies into kinetic and thermal energy are upper limits, since cooling in the hot bubble is not considered in the analytical approach.

Equations (9) and (10) from Paper I yield the kinetic and thermal energy for the SWB only. Inserting the mean value of the mechanical wind luminosity, $\langle L_w \rangle = 3.05 \times 10^{36}$ ergs s⁻¹, and adding up the results for the pure H II region, we obtain

$$\begin{aligned} E_k &= 1.6 \times 10^{50} \text{ ergs} , \\ E_i &= 2.9 \times 10^{50} \text{ ergs} , \\ E_t &= 2.6 \times 10^{50} \text{ ergs} . \end{aligned}$$

Related to the sum of Lyman continuum radiation energy and mechanical wind energy (which is almost negligible for the $35 M_\odot$ star), we get the corresponding energy transfer efficiencies according to equation (12) in Paper I:

$$\begin{aligned} \varepsilon_k &= 3.4 \times 10^{-3} , \\ \varepsilon_i &= 6.3 \times 10^{-3} , \\ \varepsilon_t &= 5.6 \times 10^{-3} . \end{aligned}$$

Comparing these values with the results of the analytical solution for the windless case and the simulations with and without wind, one can see that the increase of the kinetic energy deposit from the windless to the combined SWB/H II region simulation (almost doubled) as

well as the increase of the thermal energy deposit (also almost doubled) is about a factor of 3 below the analytical upper limits.

4.4. Comparison with Observations

In section 2 we point out the importance of X-ray observations of the hot gas in SWBs to study the physics of SWBs. Thus, we have examined the X-ray properties of our numerical model. In Figure 19 we plot the total X-ray luminosity of our model bubble in the energy band 0.1 – 2.4 keV as a function of time. The emissivity $j_\nu(\rho, T, Z)$ in each grid cell is calculated with the Raymond & Smith (1977) program. For temperatures below 10^5 K the emissivity is set to zero. The total X-ray luminosity at time t is calculated as

$$L_X(t) = \sum_{\text{cells}} \int_{h\nu=0.1 \text{ keV}}^{h\nu=2.4 \text{ keV}} 4\pi j_\nu(\rho_{\text{cell}}(t), T_{\text{cell}}(t), Z) V_{\text{cell}} d\nu, \quad (2)$$

where $\rho_{\text{cell}}(t)$ and $T_{\text{cell}}(t)$ are the plasma density and temperature in the grid cell, respectively, V_{cell} is the volume of the grid cell, and $h\nu$ the energy of the X-ray photons. For the summation over grid cells the finest grid that is available for the respective coordinates is always used. As for the calculation of all the other global quantities, the grid data are mirrored at the equator. We assume optically thin emission; absorption is neglected. For the set of chemical abundances, Z , we use the same values which Chu et al. (2003) used for their spectral X-ray fits of S308 and which are based on the abundance determination of Esteban et al. (1992) for the optically visible shell. We assume that the elements not mentioned by Chu et al. (2003) have the same abundance relative to the solar value as oxygen (0.13). Thus, for the computation of the X-ray emissivity the following elements are considered: H, He, C, N, O, Ne, Mg, Si, S, Ar, Ca, Fe, Ni with the following abundances relative to the solar values (Anders & Grevesse 1989): 1.0, 2.1, 0.1, 1.6, 0.13, 0.22, 0.13, 0.13, 0.13, 0.13, 0.13, 0.13, 0.13. This set of elemental abundances is intended to represent the chemistry in the RSG wind. The composition of the hot gas in the MS bubble may be different because the radiating material is supposed to originate from the MS wind of the star and (if thermal evaporation or ablation is important) also from the ambient medium. However, for the sake of simplicity we use the same chemical composition for all the emitting gas during the whole evolution. We will briefly discuss impacts of this choice below. The chemical composition employed for this diagnostic purpose is thus inconsistent with the solar chemical composition that is used to calculate the cooling of the gas (energy sink term in the radiation-hydrodynamical equations).

Figure 19 shows that the X-ray luminosity assumes the value 10^{32} ergs s^{-1} soon after

the turn on of the stellar wind. It remains remarkably constant during the MS phase and the associated growth of the SWB. The deviation from 10^{32} ergs s⁻¹ is less than a factor of 2.5 during this period. Most of the X-ray emission originates at the interface between the hot gas in the SWB and the swept-up H II shell. Although He and N are overabundant, the strong underabundance of the other metals reduces the X-ray luminosity. Using a solar chemical composition instead of the abundances described above would increase the luminosity in Figure 19 by a factor 3 – 4. With the onset of the RSG phase the total X-ray luminosity decreases by a factor of 3 – 4 until the star reaches the W-R stage. This happens because the hot gas (or more precisely the gas in the interface region close to the shell of swept-up ambient gas) cools and the supply of the bubble with hot gas ceases during the RSG phase.

The subsequent onset of the fast W-R wind drives up the total X-ray luminosity by approximately 3 orders of magnitude. It reaches a few times 10^{34} ergs s⁻¹, but varies quite strongly. It is interesting to note that in this phase almost all of the X-ray emission comes from the W-R shell (instead of the shocked W-R wind). At $t = 4.775$ Myr the radius of this X-ray emitting shell is approximately 10 pc with a thickness of 1.0 – 1.3 pc. The temperature drops from 2.5×10^6 K behind the shock to 6×10^5 K at the inside of the shell, the density rises from 2×10^{-25} g cm⁻³ to 1.2×10^{-24} g cm⁻³ and the velocity from 300 to 500 km s⁻¹. The shocked W-R wind has (from the reverse shock to the contact discontinuity) a density of 5×10^{-27} g cm⁻³ to 1.4×10^{-26} g cm⁻³, a temperature of 1.0×10^8 K to 5×10^7 K and a velocity of 1000 km s⁻¹ to 500 km s⁻¹. The H α emission comes mostly from the RSG shell. The density in this shell is $(3 - 12) \times 10^{-25}$ g cm⁻³, which may be seen as a lower limit since this shell is not completely resolved in our calculations. The temperature in the shell is $(8 - 20) \times 10^3$ K, indicating that there is shock heating present in addition to photoionization. The shell's velocity has slowed to 25 km s⁻¹ due to its interaction with the MS wind material.

Judging by the geometrical extent, the evolutionary state of the W-R bubble at this time is approximately comparable to the currently observable stage of S308. The model data show surprisingly good agreement with the X-ray observations of S308 described above. The total X-ray luminosity of a few times 10^{34} ergs s⁻¹ is slightly higher but of the same order of magnitude as the $\leq 1.2 \pm 0.5 \times 10^{34}$ ergs s⁻¹ observed by Chu et al. (2003). Since almost all of the X-ray emission in our model comes from the W-R shell, the temperature range of $(0.6 - 2.5) \times 10^6$ K agrees quite well with the 1.1×10^6 K that results from the spectral fit of the observed X-rays. Although the observational proof for the existence of a substantially hotter gas component is still under debate, in our model it could well be identified with the shocked, hot W-R wind which contributes only a small fraction to the total soft X-ray emission. The average density in the X-ray emitting W-R shell is $n_e \approx 0.4$ cm⁻³, which is well within the observationally determined range of $n_e = 0.28 - 0.63$ cm⁻³ for the assumed

range 0.5 – 0.1 of the hot gas volume filling factor (Chu et al. 2003). The total mass of the W-R shell is approximately $15 M_{\odot}$; i.e., most of the $18.6 M_{\odot}$ RSG wind has already been swept up. This is at the upper end of the observationally supported range of $11 \pm 5 M_{\odot}$ for an assumed volume filling factor of 0.5. The fact that the W-R shell supplies most of the X-ray emission alleviates the necessity to assume that thermal evaporation of RSG wind gas raises the mass of the X-ray emitting shocked W-R wind. The process of thermal evaporation, which is not implemented in our numerical model, would not be very efficient anyway, since the temperature gradient between the $\approx 10^6$ K W-R shell and the shocked W-R wind at several times 10^7 K is rather modest.

The conclusion of Wrigge (1999) that S308 cannot be described by the two-wind model seems to be vulnerable because he assumed that the X-ray emission originates from the shocked W-R wind and that the energy in the forward shock ahead of the W-R shell is completely dissipated in a different wavelength range. Consequently, using the formula for the X-ray luminosity of the shocked W-R wind under the impact of conductive evaporation from García-Segura & Mac Low (1995) in order to reproduce the observed X-ray luminosity, he derived values for the mechanical wind luminosity which are much too low compared to the actually observed values of the central W-R star. By contrast, the mechanical wind luminosity in our model calculation during the first 2×10^4 yr of the W-R stage is in the range $(3 - 10) \times 10^{37}$ ergs s^{-1} , which is in reasonable agreement with the observed stellar wind luminosity (scaled to the distance of $D = 1.5$ kpc used here) of 4.9×10^{37} ergs s^{-1} (Hamann et al. 1993) or 1.3×10^{37} ergs s^{-1} for a clumping-corrected mass-loss rate (Nugis et al. 1998).

Because the X-ray emitting volume is a thick shell (1.0 – 1.3 pc), another observational constraint that is well reproduced in our model is the limb brightening of the X-ray emission. In Figure 20 we display the unabsorbed angle-averaged X-ray intensity profile in the energy range 0.1 – 2.4 keV at three evolutionary times during the early W-R stage, namely $t = 4.765$ Myr, 4.770 Myr, and 4.775 Myr, the latter corresponding to the phase discussed above. We see that the “background” intensity produced by the hot gas in the MS bubble is of order 10^{-10} ergs s^{-1} cm^{-2} sr^{-1} . The intensity for lines of sight through the W-R shell is higher by 3 – 5 orders of magnitude. The limb brightening within the W-R shell can be seen for all three profiles as well as the decrease of the peak intensity with time. The consideration of absorption would not alter this result because the limb brightening is due to the geometry of the emitting plasma rather than due to varying absorption.

Since the shocked W-R wind in our model calculation has not yet swept up the entire RSG wind, the X-ray emitting shell is interior to the optical shell as has been found in the observations. Differing from Chu et al. (2003), we interpret the gap between the outer rim

of the optical emission and the outer edge of the X-ray emission as being the RSG ejecta in front of the W-R shell rather than being the W-R shell itself. The thickness of the gap in our model at this time is approximately 0.5 pc, which is smaller than the observed gap (0.7 – 1.5 pc). However, this strongly depends on the exact instant of time and on the exact duration of the RSG phase as well as the velocity of the RSG wind.

If our interpretation of the dynamical evolution is true, the age that has been attributed to the W-R bubble is probably significantly overestimated because of the assumption that the observed velocity 63 km s^{-1} is the velocity of the W-R shell rather than the velocity of the RSG shell. Based on our model the age of the bubble is $\approx 2 \times 10^4 \text{ yr}$ for the stage described above, much less than the $1.4 \times 10^5 \text{ yr}$ derived from the observed velocity of 63 km s^{-1} .

As the referee pointed out, there is no observational evidence yet of a high-velocity ($\approx 400 \text{ km s}^{-1}$) gas component that we identify as the W-R shell in our numerical results. The kinematic data obtained from the [O III] $\lambda 5007$ emission line observations of S308 and from the N V $\lambda \lambda 1239, 1243$ and C IV $\lambda \lambda 1548, 1551$ absorption line studies toward HD 50896 (Borson et al. 1997) do not show velocities as high as several 100 km s^{-1} . However, if the gas in the W-R shell of our model calculation at $T \approx 10^6 \text{ K}$ has reached collisional ionization equilibrium, oxygen exists mostly as O VII, nitrogen as N VI or N VII, and carbon as C V, C VI, or even completely ionized. Thus, there is almost no O III, N V, or C IV in the W-R shell whose emission or, respectively, absorption could be observed. Other ionic tracers are needed to find high-velocity gas of that temperature.

The appearance of NGC 6888 is harder to explain within the framework of our model. The observed geometrical size implies that the nebula is younger than S308, provided that the temporal evolution of the stellar parameters during the RSG and W-R stage is about the same. A maximum value of $\approx 8000 \text{ yr}$ can be derived under the assumptions that the optically visible nebula has not yet been swept up by the expanding W-R bubble and that our stellar model parameters are appropriate for NGC 6888. The observed X-ray luminosity $1.6 \times 10^{34} \text{ ergs s}^{-1}$ as well as the emitting plasma temperature $2 \times 10^6 \text{ K}$ (Wrigge et al. 1994) are in reasonable agreement with the model data, but the X-ray emission in the model originates from a thick shell which is more or less homogeneous rather than from small filaments with a volume filling factor of only a few %. Although the hot W-R shell is able to “hide” mass from optical observations and thus helps to find the yet undetected portion of RSG wind mass, 8000 yr after the onset of the W-R wind it contains only $\approx 3 M_{\odot}$, which is not enough to solve the problem completely (assuming that the RSG mass loss used in the model is appropriate for NGC 6888). The biggest difficulty is probably the appearance of the optical shell. In the numerical model the RSG shell already has a radius greater than 10 pc and the unaffected RSG wind between the W-R shell and the RSG shell

contributes significantly to the $H\alpha$ emission. This conflicts with the observation of a very thin, filamentary shell with hydrogen number densities as high as 1000 cm^{-3} .

There may be various reasons for this mismatch between our model and the observations of NGC 6888. It is possible that physical effects not yet covered in our model are more important for NGC 6888 or that the resolution applied in our calculations is not yet high enough to allow for the formation of high-density filaments. Another possibility is that the actual mass-loss history of HD 192163 differs from what is expected and used in our calculations.

Apart from the detailed comparison, Figure 19 illustrates another aspect: The fact that up to now only W-R bubbles have been observed in X-rays is not only by chance. At least for the MS \rightarrow RSG \rightarrow W-R sequence the X-ray luminosity during the final W-R stage exceeds that of the rest of the stellar lifetime by more than an order of magnitude. Moreover, during the early W-R phase the emission comes from a relatively small volume (compared to most of the MS lifetime), resulting in an even higher X-ray surface brightness, which is easier to detect.

5. Summary and Conclusions

The basic difference between the simulations presented in this paper and those of Paper I is the choice of the stellar parameters, which here are chosen to model a $35 M_{\odot}$ star that undergoes the evolution from the MS through the RSG and W-R stages. The fundamental structures which evolve are basically the same as observed in the $60 M_{\odot}$ case. They are generally smaller because for most of the time the stellar wind luminosity and the Lyman continuum luminosity are lower than in the $60 M_{\odot}$ case. At the end of the simulation the entire bubble structure has a radius of $\approx 44 \text{ pc}$, which is some 6 pc smaller than the final bubble of the $60 M_{\odot}$ case, although the $35 M_{\odot}$ star lives 0.88 Myr longer than the $60 M_{\odot}$ star.

Instability-driven structure formation during the early MS phase of the star (the formation of ionized fingers corrugating the ionization front and the formation of neutral spokes shadowed by dense clumps), which we found to be quite prominent in the case of the $60 M_{\odot}$ calculation, is also visible in the calculations presented here, but it is much less pronounced and only short-lived, because of the lower mechanical wind luminosity of the star. The lower mechanical wind luminosity of the star reduces the thermal pressure of the hot gas in the bubble. The lower pressure in the hot bubble increases the geometrical thickness of the shell of swept-up H II gas, making it less sensitive to thin-shell instabilities that could trigger the

formation of the morphological structures described above. Since this behavior better preserves the basic spherical structure, other morphological effects become visible, which might be prohibited in the $60 M_{\odot}$ case by the strong corrugation of the bubble shell: When the swept-up H II shell broadens geometrically, the plasma density in the shell decreases. This rarefaction reduces the rate of Lyman continuum photons necessary to sustain the photoionization of the shell and excess photons become available, which drive the ionization front outward and photoevaporate additional material from the neutral shell of swept-up ambient medium. The inward flow of evaporated material collides with the outward flow of the dissolving swept-up H II shell, temporarily forming a new shell of enhanced density. Since all the plasma within the H II region is almost isothermal, this density fluctuation vanishes soon.

Another consequence of the reduced stellar wind luminosity (compared to the $60 M_{\odot}$ case) is the fact that for most of the time the shape of the H II region is more or less preserved as a broad shell interior to the thin shell of swept-up ambient material rather than being so thin as in the $60 M_{\odot}$ case where the H II region is compressed into the illuminated inner part of the outer shell. Nevertheless, the geometrical thickness of the photoionized shell shrinks at the end of the simulation when the stellar wind luminosity reaches its maximum during the final W-R stage.

The morphological impact of the low-velocity mass-loss phase (the RSG stage) is more prominent than that of the $60 M_{\odot}$ star (the LBV stage), because the total mass loss during the RSG stage is higher ($\approx 18.6 M_{\odot}$) than during the LBV stage of the $60 M_{\odot}$ star ($\approx 7.3 M_{\odot}$). The slowly expanding RSG wind material is subsequently swept up and accelerated by the shocked W-R wind so that Rayleigh-Taylor instabilities break it into filaments.

The final, pre-supernova structure that shows up in the $35 M_{\odot}$ case after 4.945 Myr is basically comparable to that of the $60 M_{\odot}$ case at its end. The entire bubble is slightly smaller, the H II shell at the inside of the outer neutral swept-up shell is more extended than in the $60 M_{\odot}$ case. Outer shell and H II region are less clumpy and show less rippling as a consequence of the different evolutionary scenarios.

The reduced substructure formation during the early MS phase is also reflected in the circumstellar energetics. The decrease of ionization energy and thermal energy of warm gas (compared to the respective case without stellar wind) resulting from the formation of dense photoionized structures with short recombination times is smaller than for the $60 M_{\odot}$ case. Ionization energy dominates the energy in the circumstellar gas for most of the evolution. The kinetic energy of bulk motion as well as the warm and the hot component of thermal energy stay fairly close together from $t \approx 0.3$ Myr until the star enters the RSG phase.

The energetic variations during the RSG stage are stronger than those during the LBV stage of the $60 M_{\odot}$ star because, due to the duration of the RSG phase, the ionizing radiation of the star is switched off for a considerable period of time so that the photoionized regions recombine. In addition, the mass that is ejected during the RSG stage and accelerated during the subsequent W-R stage is about 2.5 times higher than the mass ejected during the LBV stage of the $60 M_{\odot}$ star.

At the end of the $35 M_{\odot}$ simulation the total energy transfer efficiency is 1%. This value is about the same as in the corresponding case without stellar wind, but it is 2.7 times higher than the value at the end of the $60 M_{\odot}$ simulation. 54% of the net energy which has been added to the system is then in the form of ionization energy, 36% in thermal energy and 10% in kinetic energy of bulk motion. The corresponding values at the end of the $60 M_{\odot}$ calculation are 25%, 40%, and 35%, respectively. This is another indication that the stellar wind plays a more prominent role in the $60 M_{\odot}$ case.

Remarkable agreement of the X-ray properties is found when comparing our model calculations during the early W-R phase with observations of S308. The order of magnitude of the observed X-ray luminosity as well as the temperature of the emitting plasma and the limb brightening of the intensity profile are well reproduced. The obvious explanation that our model overcomes the “missing wind problem” described in § 2 is that almost the entire X-ray emission during this phase comes from the W-R shell rather than from the shocked W-R wind. Analytical models constructed so far (see e.g. García-Segura & Mac Low 1995) assume the W-R shell to be thin and cool so that the energy in the forward shock is completely dissipated in the low-energy wavelength range. The source of X-rays in these models is the shocked W-R wind and the efficiency of heat conduction and thermal evaporation between the hot gas and the cold W-R shell strongly influences the luminosity and the spectral shape of the X-ray emission. If heat conduction is efficient enough to cool the hot shocked W-R wind down to the observed temperature and if the W-R wind luminosity in the models is adjusted to reproduce the observed X-ray luminosity, the W-R wind luminosity is usually much lower than observed (Wrigge 1999).

Another factor that reduces the X-ray luminosity in our model to values roughly comparable with S308 is the assumed set of chemical abundances. Although He and N are overabundant according to the observations in the nebula, the underabundance of the other metals reduces the X-ray luminosity by a factor of 3 – 4 compared to what can be expected from solar chemical composition.

A further consequence of this interpretation of our results is that the $H\alpha$ emission originates mostly from the RSG shell. This is in agreement with the finding of Chu et al. (2003) that the X-ray emission is completely interior to the optical shell. Since the age

of S308 (and other W-R bubbles) was hitherto derived from the expansion velocity of the optical nebula under the assumption that the nebula is part of the W-R shell, our results imply an age of S308 which is much younger ($\approx 2 \times 10^4$ yr) than assumed so far.

However, the match of our model data and the observations is worse for the case of NGC 6888. Besides numerical or model restrictions, differences of the mass-loss and luminosity history between the central star of NGC 6888 and our model star might be responsible for the discrepancies.

This work was supported by the Deutsche Forschungsgemeinschaft (DFG) under grant number He 1487/17 and by the National Aeronautics and Space Administration (NASA) under grant NRA-03-OSS-01-TPF. Part of the research described in this paper was conducted at the Jet Propulsion Laboratory (JPL), California Institute of Technology. The computations were performed at the Rechenzentrum der Universität Kiel, the Konrad-Zuse-Zentrum für Informationstechnik in Berlin, and the John von Neumann-Institut für Computing in Jülich. We thank the referee, Guillermo García-Segura, for valuable comments and for making available new kinematic data of S308.

REFERENCES

- Anders, E., & Grevesse, N. 1989, *Geochim. Cosmochim. Acta*, 53, 197
- Arnal, E. M., & Cappa, C. E. 1996, *MNRAS*, 279, 788
- Bochkarev, N. G. 1988, *Nature*, 332, 518
- Boroson, B., McCray, R., Clark, C. O., Slavin, J., Mac Low, M.-M., Chu, Y.-H., & Van Buren, D. 1997, *ApJ*, 478, 638 (erratum 485, 436)
- Chu, Y.-H. 1981, *ApJ*, 249, 195
- Chu, Y.-H. 1982, *ApJ*, 254, 578
- Chu, Y.-H., Guerrero, M. A., Gruendl, R. A., García-Segura, G., & Wendker, H. J. 2003, *ApJ*, 599, 1189
- Chu, Y.-H., Gull, T. R., Treffers, R. R., Kwitter, K. B., & Troland, T. H. 1982, *ApJ*, 254, 562
- Crowther, P. A., & Smith, L. J. 1996, *A&A*, 305, 541

- Esteban, C., & Vílchez J. M. 1992, ApJ, 390, 536
- Esteban, C., Vílchez, J. M., Smith, L. J., & Clegg, R. E. S. 1992, A&A, 259, 629
- Firmani, C., Koenigsberger, G., Bisiacchi, G. F., Ruiz, E., & Solar, A. 1979, in IAU Symp. 83, Mass Loss and Evolution of O-Type Stars, ed. P. S. Conti, & C. W. H. de Loore (Dordrecht: Reidel), 421
- Freyer, T., Hensler, G., & Yorke, H. W. 2003, ApJ, 594, 888 (Paper I)
- García-Segura, G., Langer, N., & Mac Low, M.-M. 1996, A&A, 316, 133
- García-Segura, G., & Mac Low, M.-M. 1995, ApJ, 455, 145
- Gruendl, R. A., Chu, Y.-H., Dunne, B. C., & Points, S. D. 2000, AJ, 120, 2670
- Hamann, W.-R., Koesterke, L., & Wessolowski, U. 1993, A&A, 274, 397
- Hamann, W.-R., Schmutz, W., & Wessolowski, U. 1988, A&A, 194, 190
- Howarth, I. D., & Schmutz, W. 1995, A&A, 294, 529
- Johnson, H. M., & Hogg, D. E. 1965, ApJ, 142, 1033
- Kwitter, K. B. 1981, ApJ, 245, 154
- Marston, A. P. 1991, ApJ, 366, 181
- Marston, A. P. 1995, AJ, 109, 2257
- Marston, A. P., & Meaburn, J. 1988, MNRAS, 235, 391
- Moore, B. D., Hester, J. J., & Scowen, P. A. 2000, AJ, 119, 2991
- Nugis, T., Crowther, P. A., & Willis, A. J. 1998, A&A, 333, 956
- Parker, R. A. R. 1964, ApJ, 139, 493
- Perryman, M. A. C., et al. 1997, A&A, 323, L49
- Raymond, J. C., & Smith, B. W. 1977, ApJS, 35, 419
- Treffers, R. R., & Chu, Y.-H. 1982, ApJ, 254, 569
- Van Buren, D., & McCray, R. 1988, ApJ, 329, L93
- van der Hucht, K. A. 2001, NewA Rev., 45, 135

Weaver, R., McCray, R., Castor, J., Shapiro, P., & Moore, R. 1977, ApJ, 218, 377; erratum, 220, 742

Wendker, H. J., Smith, L. F., Israel, F. P., Habing, H. J., & Dickel, H. R. 1975, A&A, 42, 173

Wrigge, M. 1999, A&A, 343, 599

Wrigge, M., & Wendker, H. J. 2002, A&A, 391, 287

Wrigge, M., Wendker, H. J., & Wisotzki, L. 1994, A&A, 286, 219

Yorke, H. W., & Kaisig, M. 1995, Comput. Phys. Commun., 89, 29

Yorke, H. W., & Welz, A. 1996, A&A, 315, 555

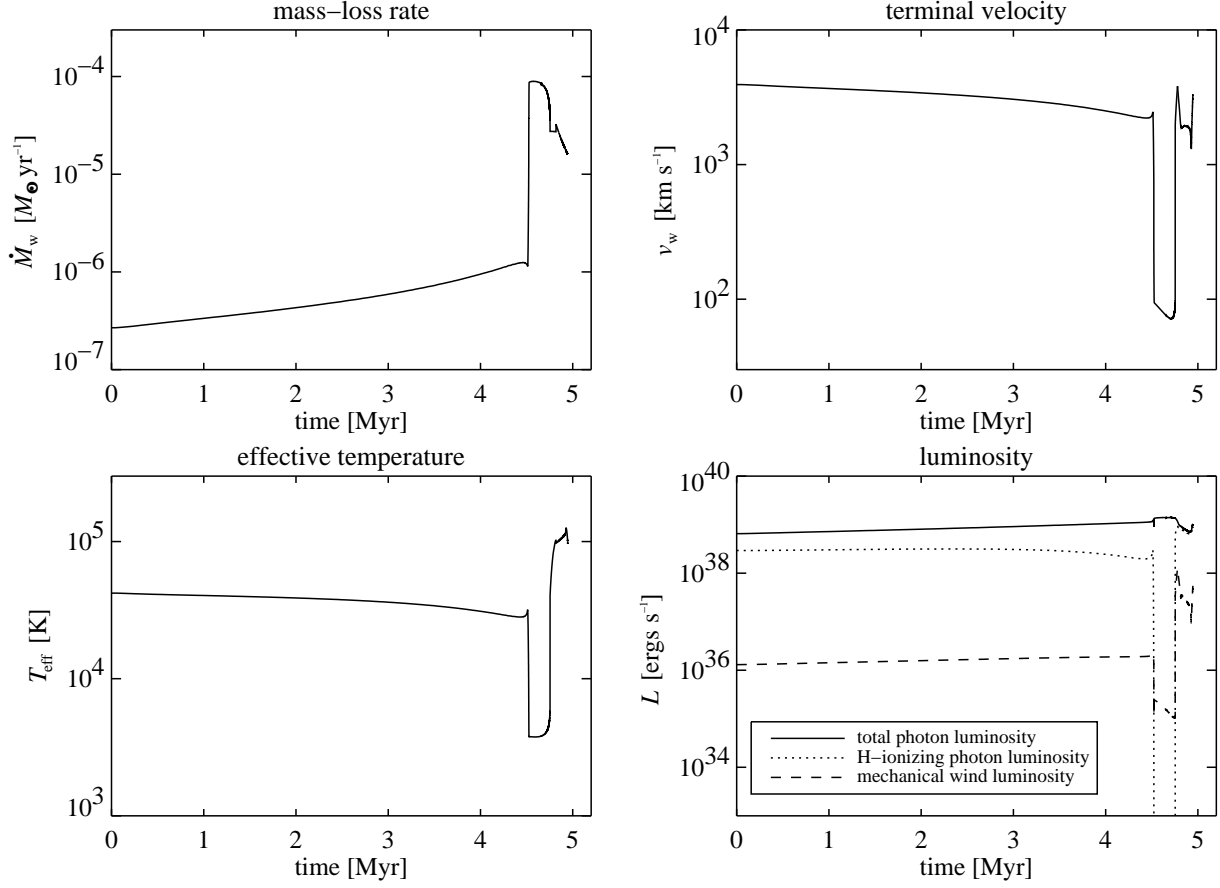


Fig. 1.— Time-dependent stellar parameters used as boundary conditions for the calculation of the $35 M_{\odot}$ case: mass-loss rate (*top left*), terminal velocity of the wind (*top right*), effective temperature (*bottom left*), and luminosity (*bottom right*). All parameters are adopted from García-Segura et al. (1996).

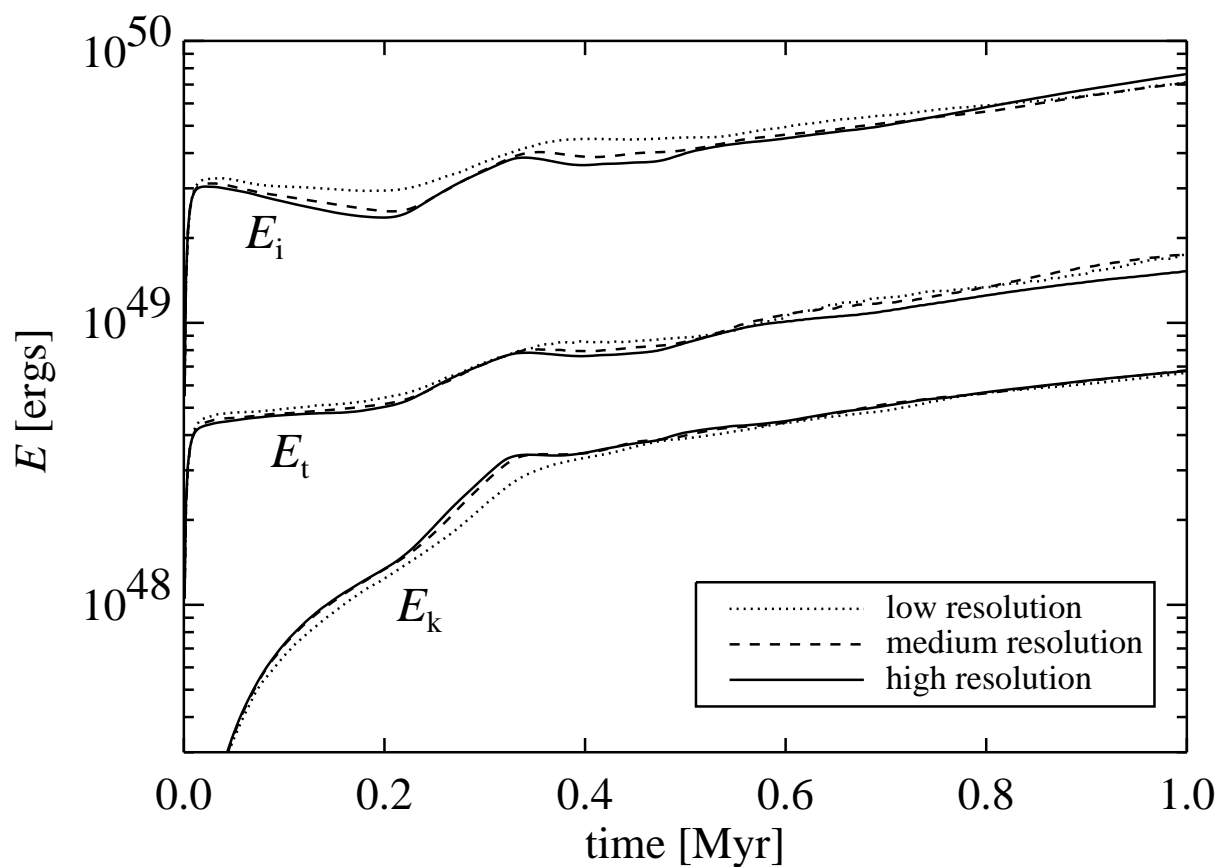


Fig. 2.— Resolution study for the $35 M_{\odot}$ case. E_k is the total kinetic energy of bulk motion in the system, E_t the thermal energy, and E_i the ionization energy (13.6 eV per ionized hydrogen atom).

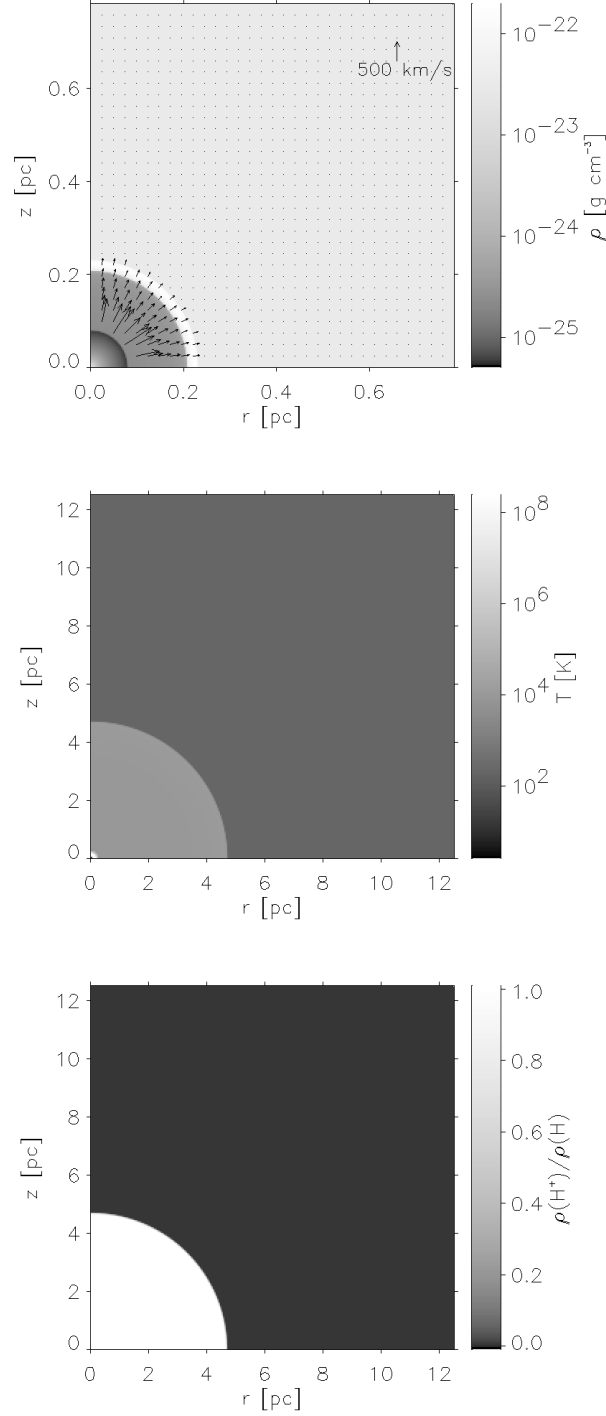


Fig. 3.— Circumstellar mass density and velocity field (*top*), temperature (*middle*), and degree of hydrogen ionization (*bottom*) for the $35 M_{\odot}$ case at evolutionary age 700 yr (high-resolution run). The velocity arrows in the free-flowing wind zone have been omitted to prevent confusion. The star is located in the center of the coordinate system. Note the different length scales.

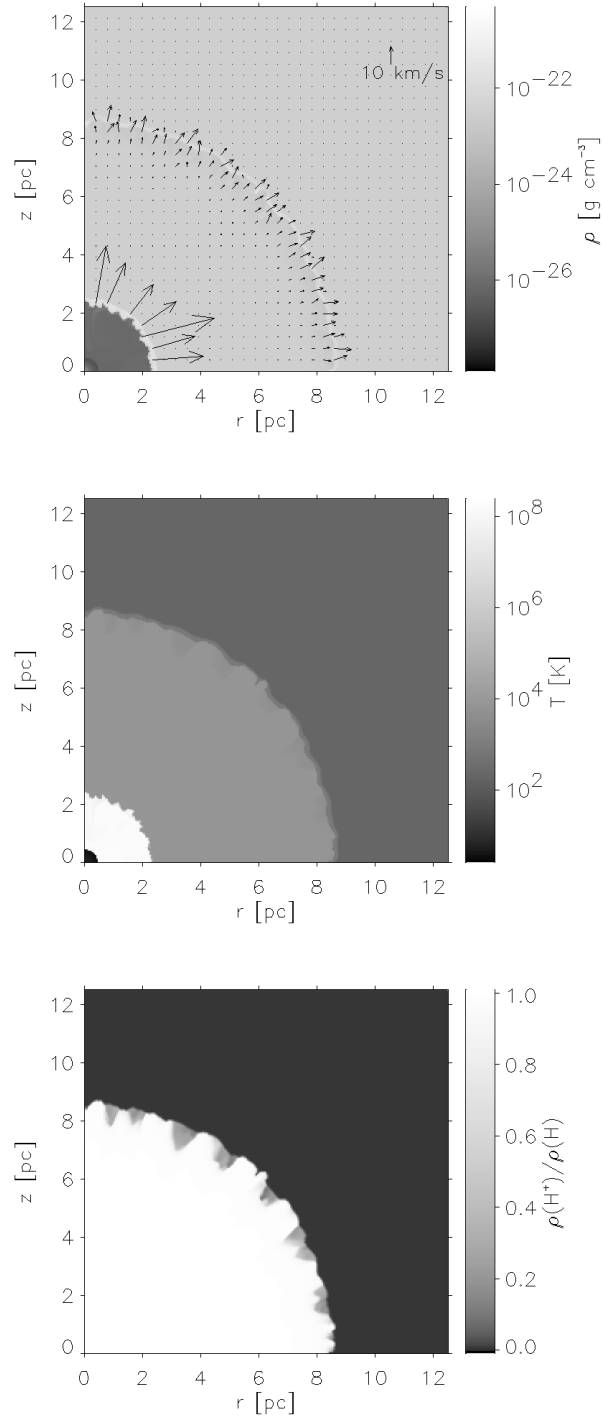


Fig. 4.— Same as Fig. 3, but at age 5×10^4 yr. The velocity arrows in the free-flowing wind zone and in the hot bubble have been omitted to prevent confusion.

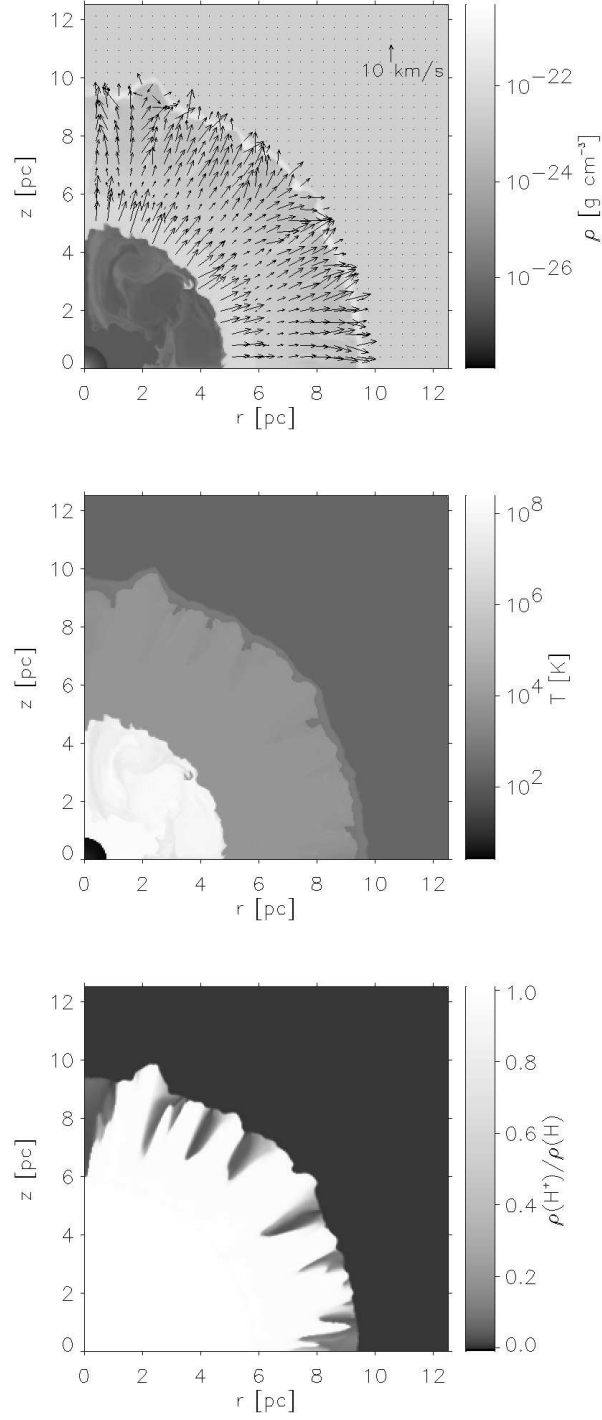


Fig. 5.— Same as Fig. 4, but at age 0.2 Myr

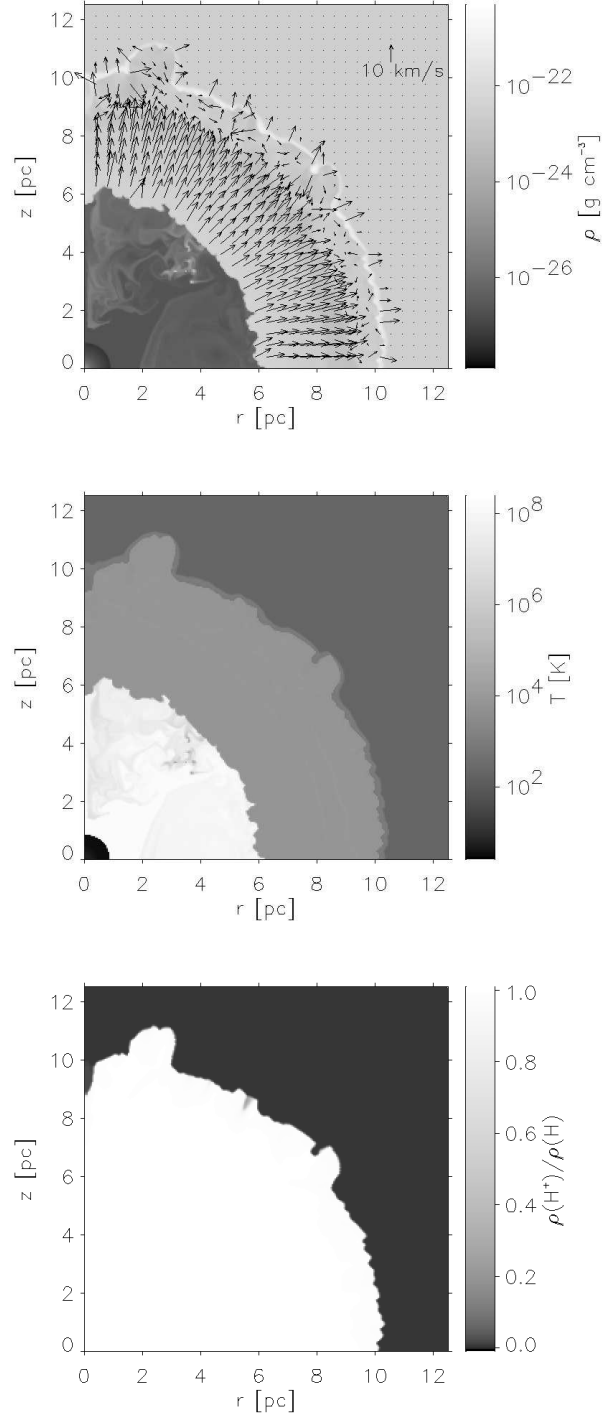


Fig. 6.— Same as Fig. 4, but at age 0.3 Myr

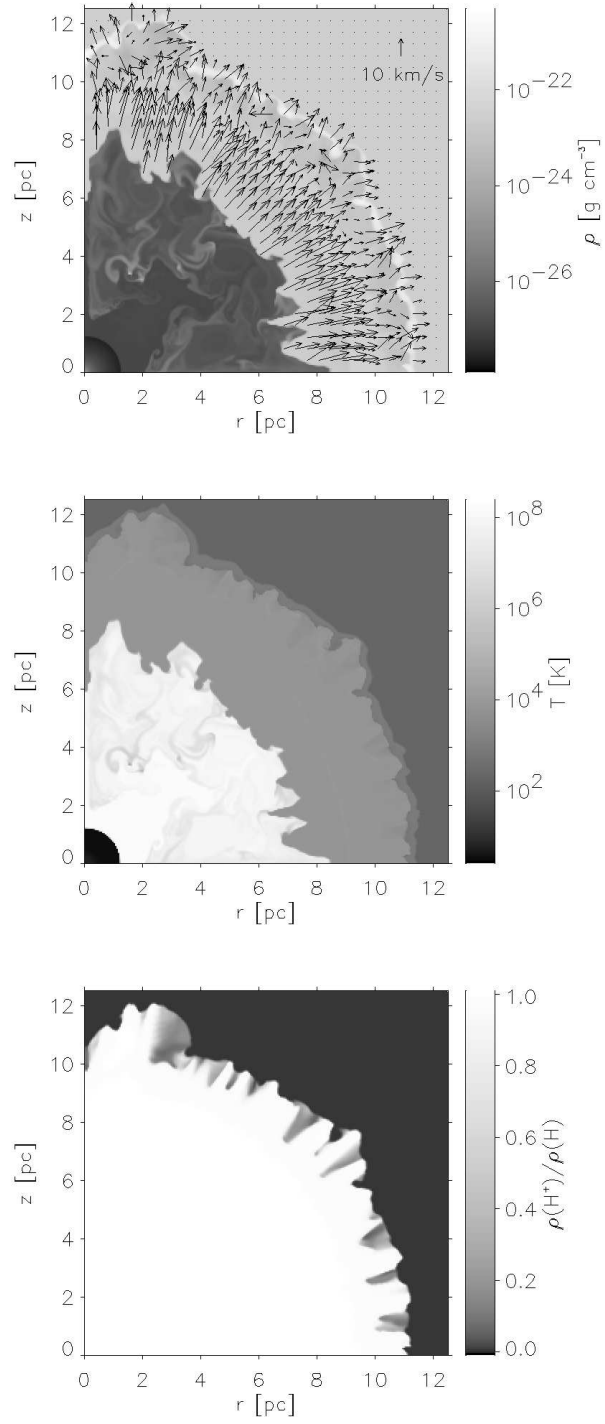


Fig. 7.— Same as Fig. 4, but at age 0.4 Myr

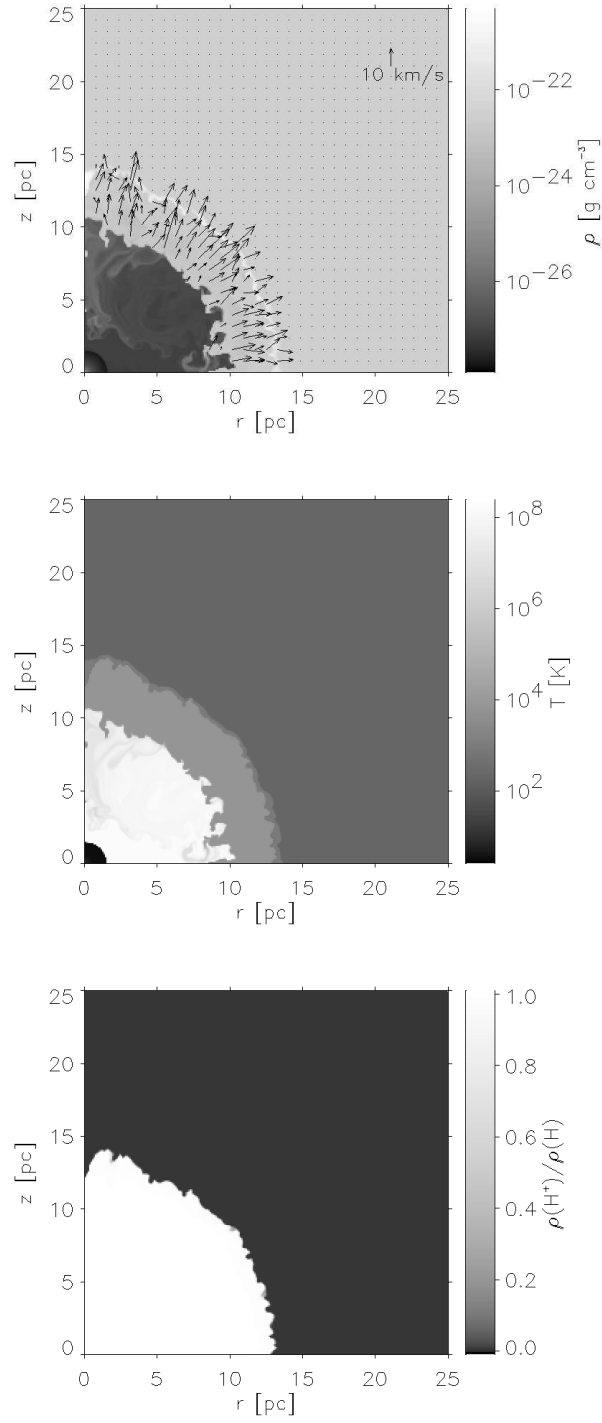


Fig. 8.— Same as Fig. 4, but at age 0.6 Myr. Because of the bubble expansion, a larger volume is shown.

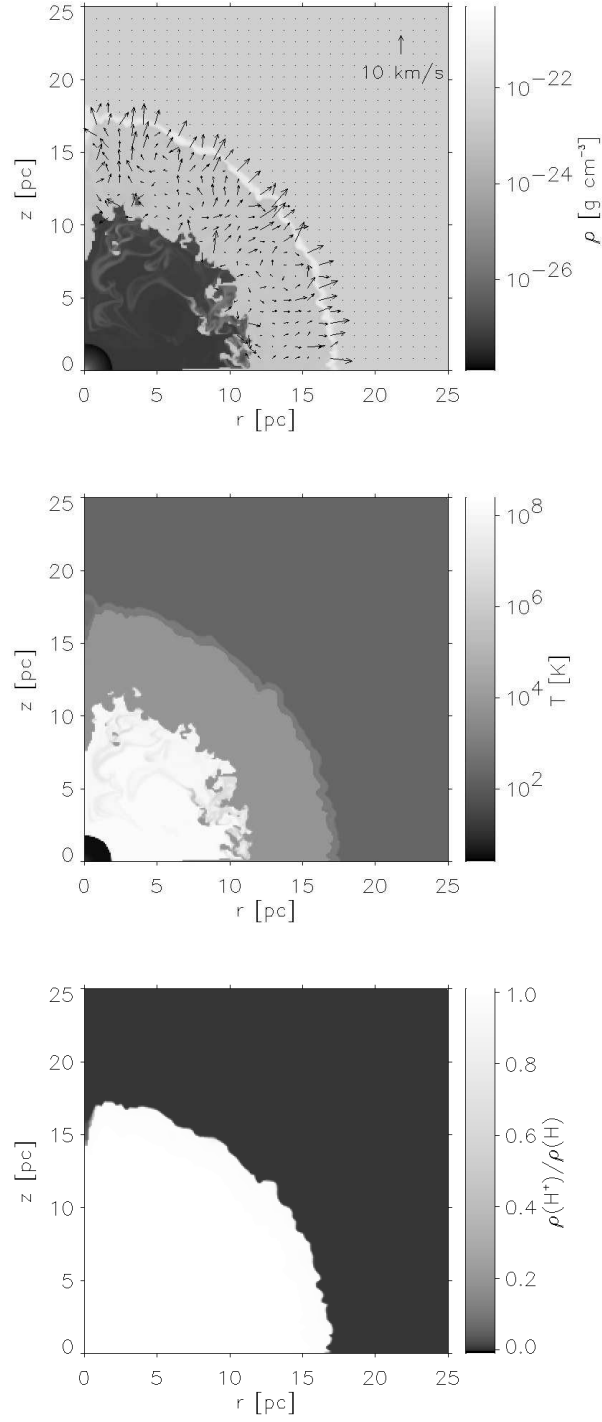


Fig. 9.— Same as Fig. 8, but at age 1.0 Myr

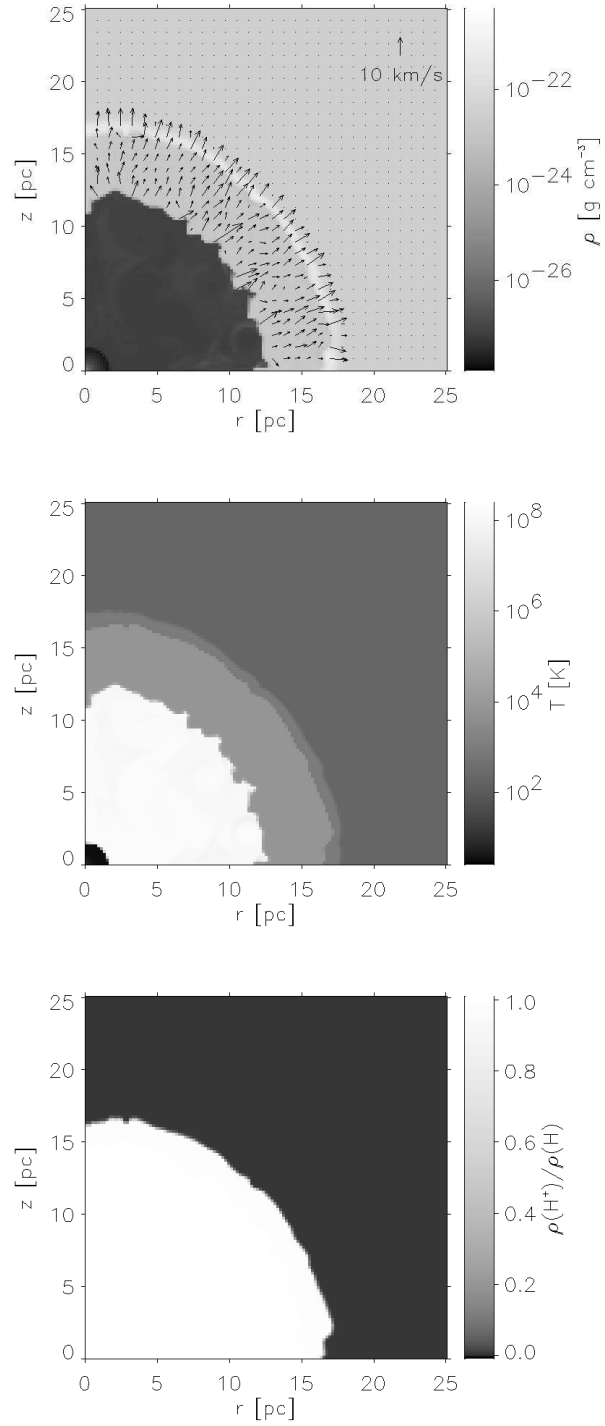


Fig. 10.— Same as Fig. 9, but for the medium-resolution run

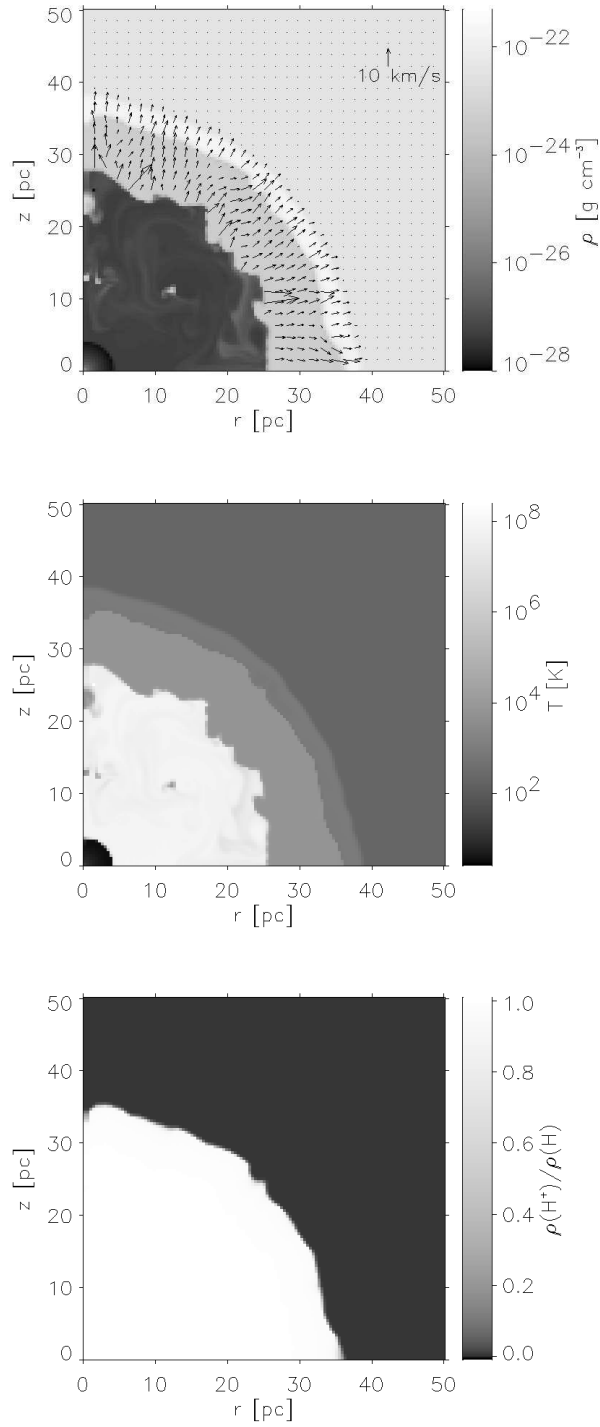


Fig. 11.— Same as Fig. 10, but at age 4.0 Myr, and the displayed area is enlarged once again

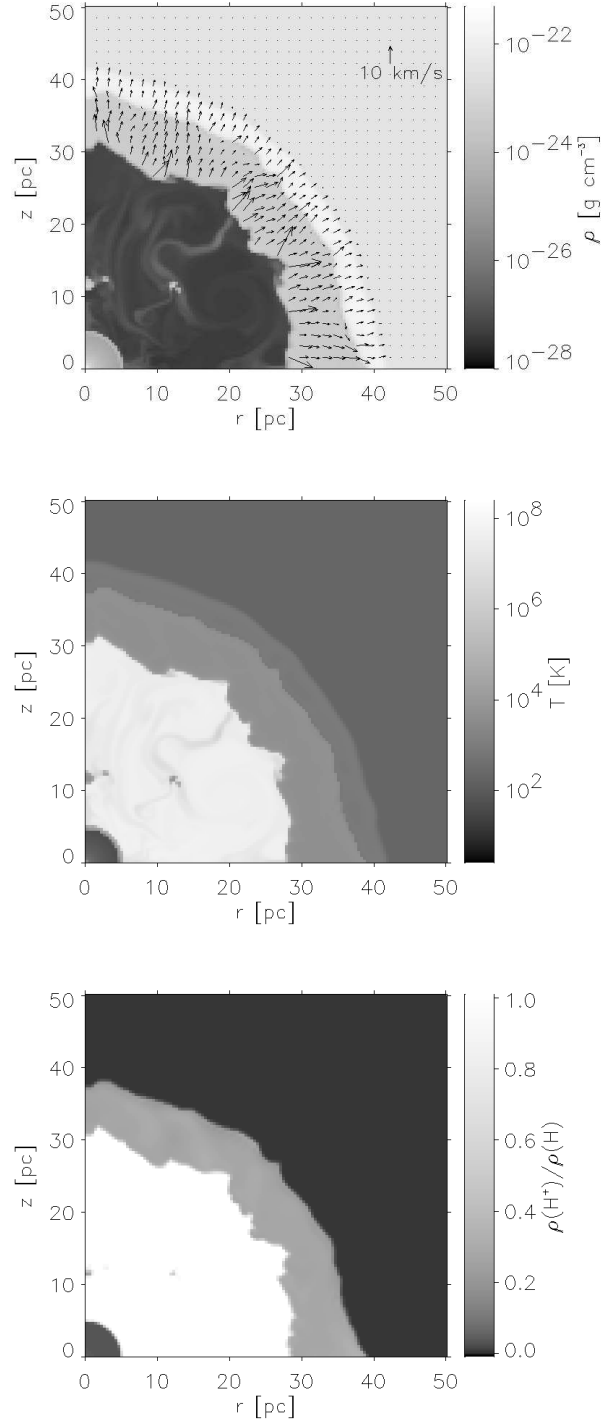


Fig. 12.— Same as Fig. 11, but at age 4.59 Myr

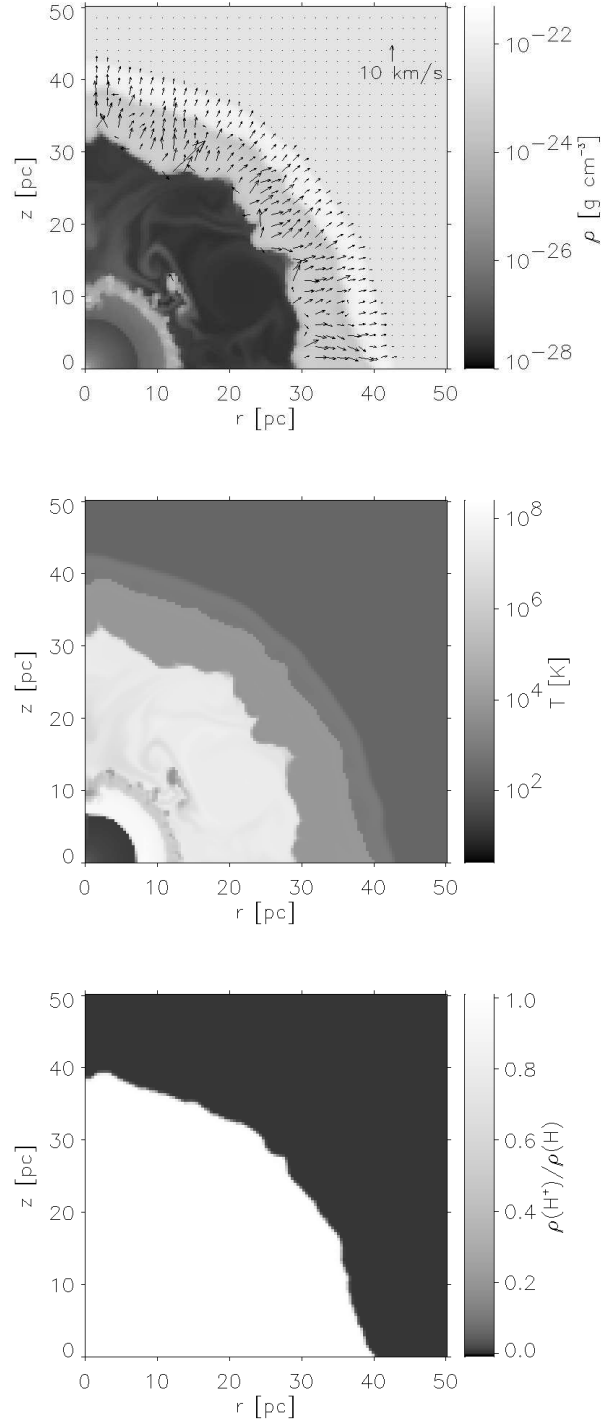


Fig. 13.— Same as Fig. 11, but at age 4.78 Myr

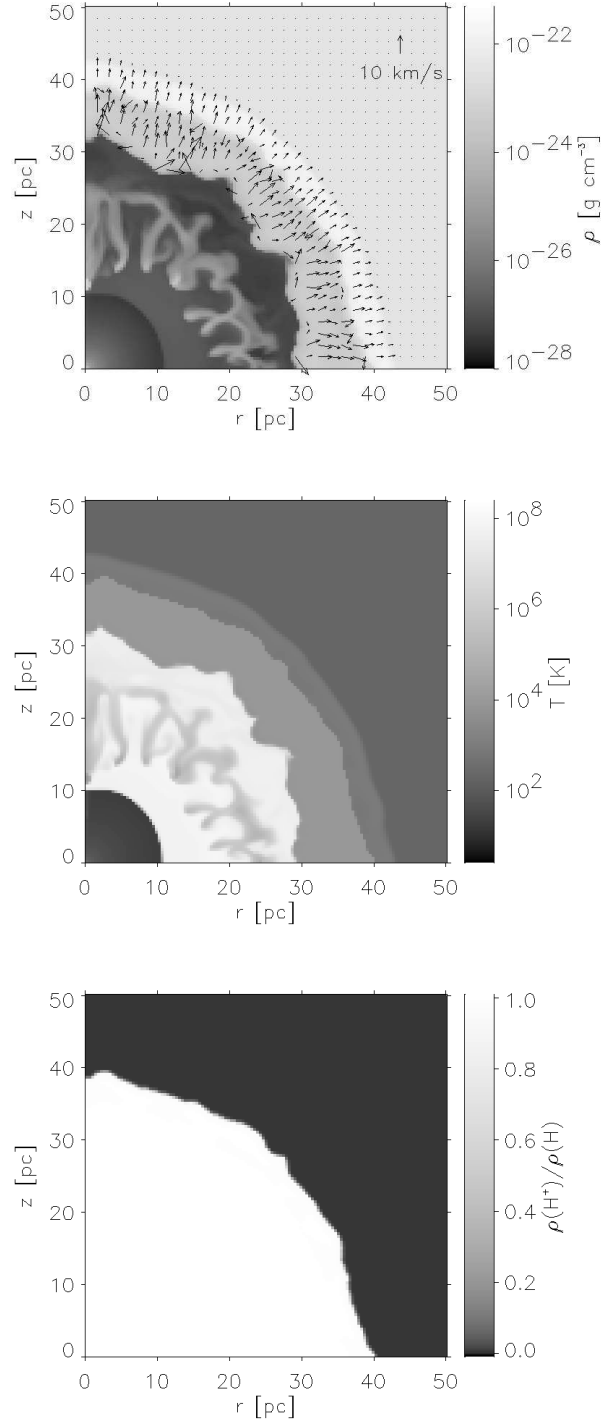


Fig. 14.— Same as Fig. 11, but at age 4.80 Myr

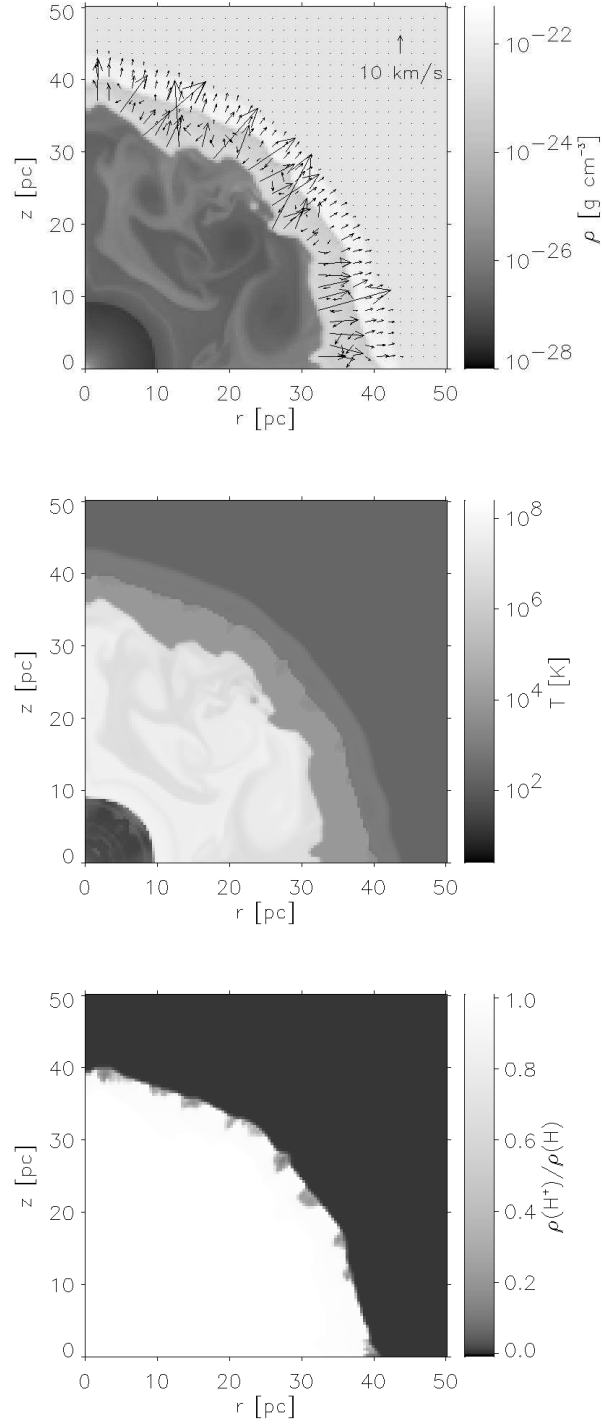


Fig. 15.— Same as Fig. 11, but at age 4.945 Myr

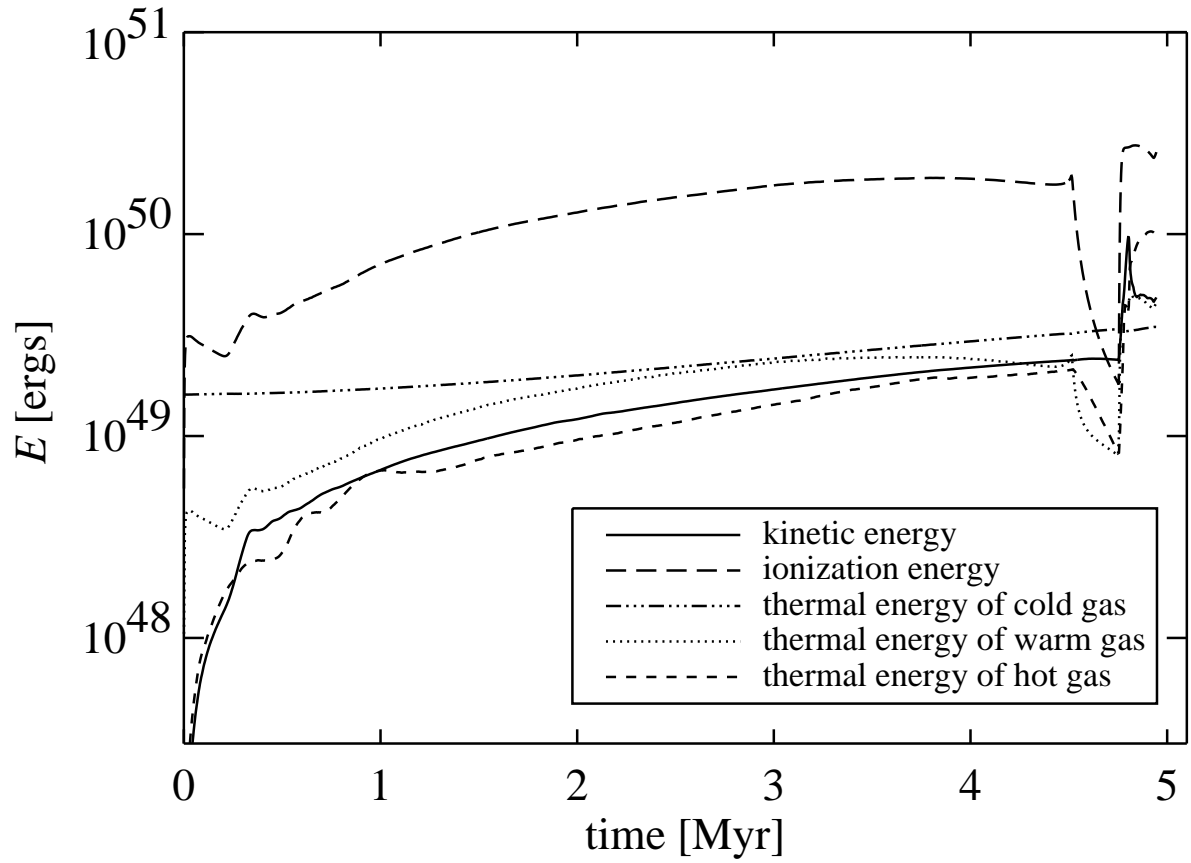


Fig. 16.— Temporal evolution of kinetic, thermal, and ionization energy for the $35 M_{\odot}$ case. For details see text.

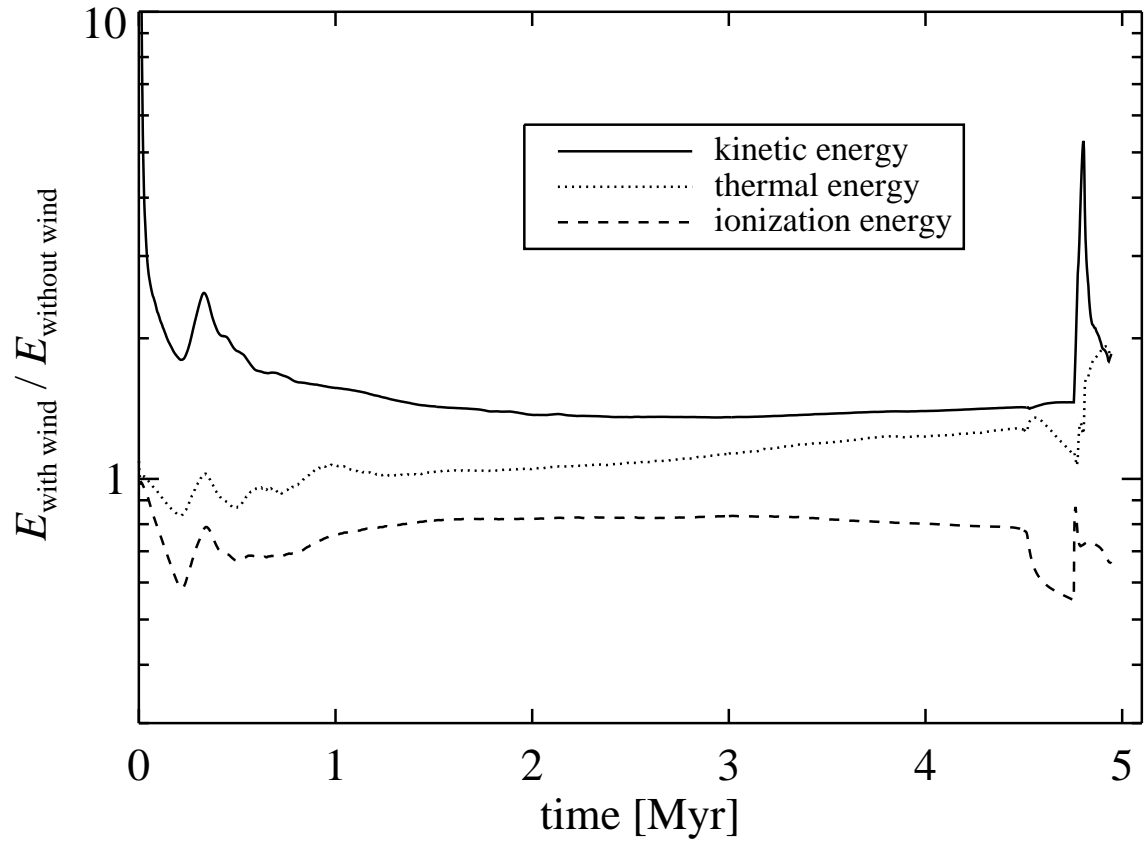


Fig. 17.— Ratio of energies for the $35 M_{\odot}$ case with and without a stellar wind.

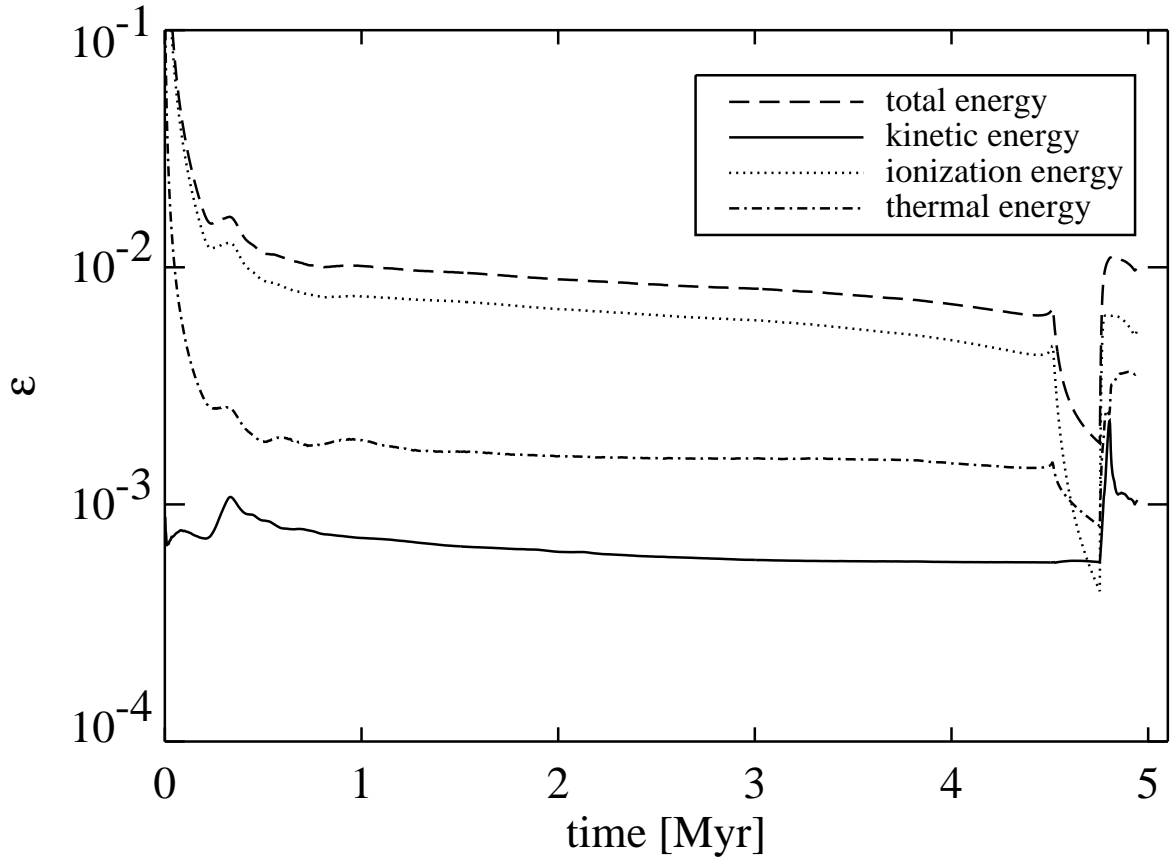


Fig. 18.— Energy transfer efficiency with respect to the total energy input for the $35 M_{\odot}$ case.

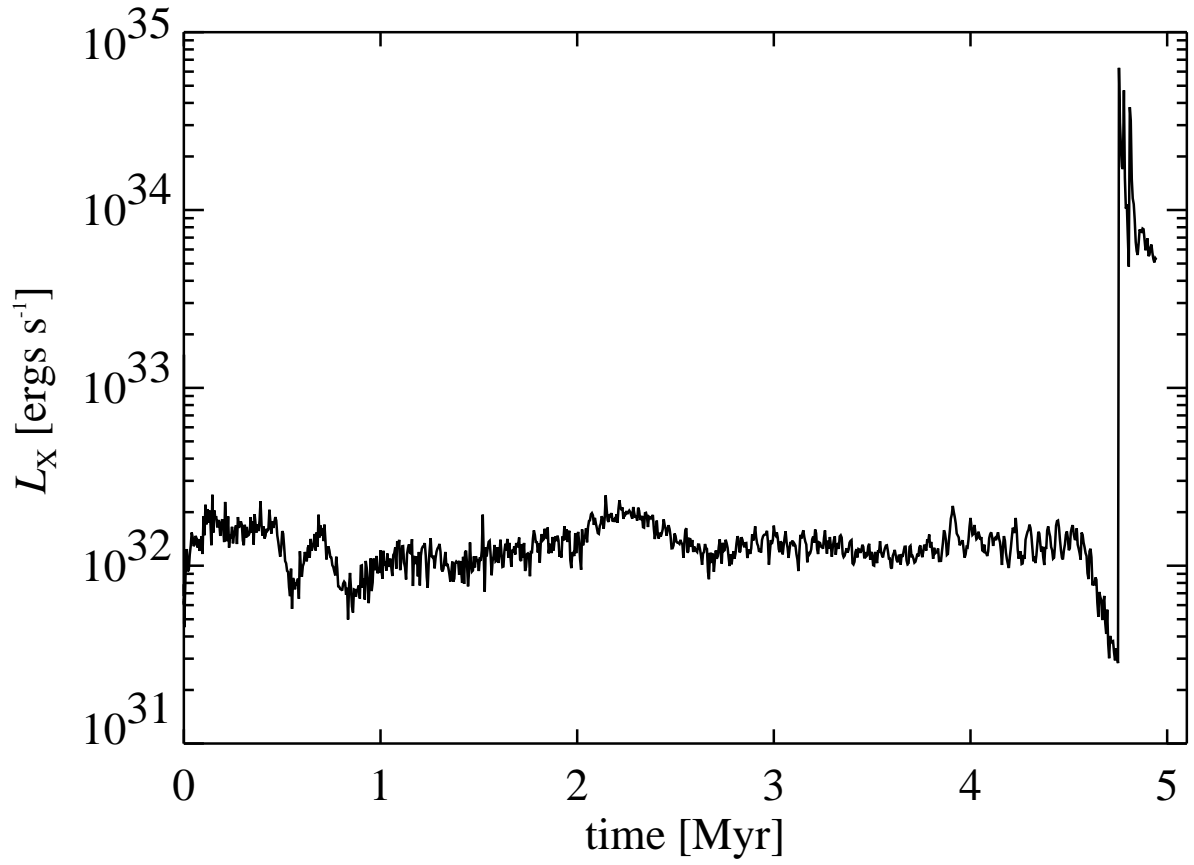


Fig. 19.— X-ray luminosity in the energy band 0.1 – 2.4 keV for the 35 M_{\odot} case with stellar wind.

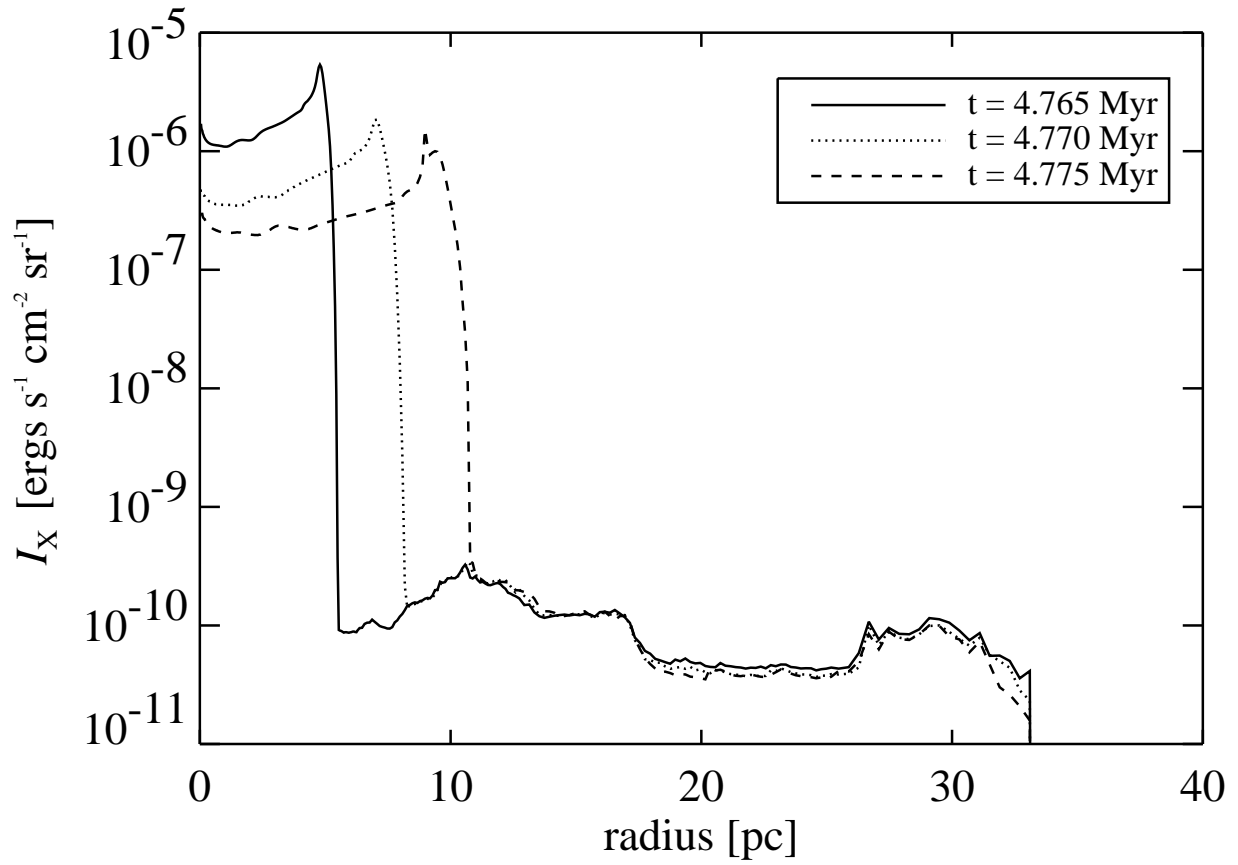


Fig. 20.— Angle-averaged unabsorbed X-ray intensity in the energy band 0.1 – 2.4 keV for the $35 M_{\odot}$ case with stellar wind at selected evolutionary times.

Table 1: Energy Components at the End of the 35 M_{\odot} Simulations

Model Parameters	E_k ($\times 10^{49}$ ergs)	E_i ($\times 10^{49}$ ergs)	$E_{t,cold}$ ($\times 10^{49}$ ergs)	$E_{t,warm}$ ($\times 10^{49}$ ergs)	$E_{t,hot}$ ($\times 10^{49}$ ergs)
Windless	2.6	39	3.0	7.6	0
With wind	4.9	25	3.5	4.3	11

Note. — The thermal energy of the cold component, $E_{t,cold}$, contains the internal energy of the initially unperturbed ambient medium (1.6×10^{49} ergs) that has to be subtracted whenever the input of thermal energy into the system is considered.

Table 2: Energy Transfer Efficiencies at the End of the $60 M_{\odot}$ and $35 M_{\odot}$ Simulations

Model Parameters	ε_k ($\times 10^{-4}$)	ε_i ($\times 10^{-4}$)	ε_t ($\times 10^{-4}$)	ε_{tot} ($\times 10^{-4}$)
$60 M_{\odot}$ windless	3.3	12	6.4	22
$60 M_{\odot}$ with wind	13	9.1	15	37
$35 M_{\odot}$ windless	5.7	84	19	109
$35 M_{\odot}$ with wind	10	55	36	101

Note. — The data of the $60 M_{\odot}$ case are taken from Paper I.